3. Structural and spectroscopic characterisation

Introduction

The target of this chapter is to present an investigation into the structural and spectroscopic properties of pure and catalysed nanocrystalline WO_3 powder. It is well known how important is to control and investigate the microstructure of the sensing materials in order to understand and improve the performance of sensor devices. Therefore, this chapter reports on those characteristics that may be important for the application of this material in the field of gas sensors. This goal can only be achieved if a *multitechnique* approach is taken, as many conclusions can only be reached with the aid of more than one characterisation technique. The chapter is divided into two main parts covering the characterisation of pure and catalysed WO_3.

The first part of the chapter deals with the characterisation of pure nanocrystalline WO_3 powders. The main parameter analysed is the influence of annealing on the structural properties. As already mentioned, some features can only be fully understood after contrasting different characterisation techniques. That is why results concerning each characterisation technique are firstly presented. In these subsections, only results and their direct interpretation are provided. Finally, a discussion section intends to clarify and correlate the different results obtained.

Structural and spectroscopic properties of catalysed WO_3 are reported in the second part of the chapter. In this case, the emphasis lays on the characterisation of catalytic centres, rather than on bulk WO_3. Due to the low concentration of the additives introduced, only a few techniques are really useful for their characterisation. This section is divided into three main parts corresponding to the different additives introduced: copper, vanadium and chromium.

3.1 Pure nanocrystalline WO_3 powder

3.1.1 Results of the characterisation

3.1.1.1 X-ray diffraction

Dried gels (also called *as-obtained WO_3* hereafter) were obtained after heating the dissolution of tungstic acid in methanol and water at 80ºC and evaporate the solvent at 110ºC as explained in Chapter 2. In Fig. 1, XRD spectra of commercial tungstic acid and as-obtained WO_3 are compared. As-obtained WO_3 presents a main peak at 2θ=24.2º. This corresponds to the peak (200) of WO_3 in triclinic structure (JCPDS card no. 20-1323). As stated in Chapter 1, crystalline WO_3 presents a pseudocubic structure with a slight distortion of the cubic ReO_3-type lattice, being monoclinic and triclinic the most common structures at ambient temperature [1-3]. However, it is interesting to notice as-obtained WO_3 still presents small peaks at 2θ=16.5º and 2θ=25.6º. Tungsten oxide hydrates ($WO_3 \cdot nH_2O$) present main peaks at 2θ=16.5º and 2θ=25.7º (JCPDS card no. 43-0679). Since tungsten oxide hydrate is an intermediate product between tungstic acid and tungsten oxide [2], it is reasonable to assign these reflections to tungsten oxide hydrate. Therefore, dried gels should be identified as WO_3 with a small amount of $WO_3 \cdot nH_2O$.

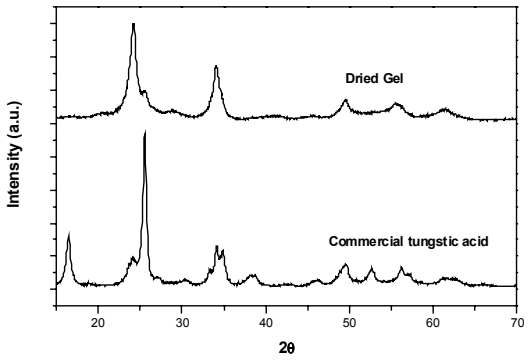

Fig. 1: *Comparison of the XRD spectra of commercial tungstic acid and dried gel obtained*

Annealed powder was identified by XRD as nanocrystalline WO_3. Monoclinic structure is described in the *P21/n* space with cell parameters a = 0.7301 nm, b = 0.7539 nm, c = 0.7689 nm, and β = 90.89°. The triclinic structure is described in the *P-1* space group with cell parameters a = 0.7310 nm, b = 0.7524 nm, c = 0.7686 nm, α = 88.85°, β = 90.91°, γ = 90.935°. Fig. 2 presents XRD patterns from 2θ=20º to 40º of WO_3 samples annealed at different temperatures (400ºC, 500ºC, 600ºC and 700ºC). This figure also includes theoretical diffraction diagrams of the triclinic and monoclinic compounds. These diagrams have been calculated using the program FULLPROF [4], taking the cell parameters and

atomic positions of ref. [3] and an artificial crystallite size of 50 nm. Due to the slight distortion of the lattice, the main reflection (100) of the ideal cubic cell splits in three in the range 20-30º [20]: (100), (010) and (001) pseudo-cubic reflections. It is clear from Fig.2 these three main reflections can not be used to determine if the crystalline structure is triclinic or monoclinic, since their position and relative intensity is very similar for both structures when dealing with nanometric grain sizes. However, it is interesting to notice the evolution of maximum intensity and the Full Width at Half Maximum (FWHM) with annealing temperature of these three main peaks, shown in Fig. 3. Intensities of the three main reflections should be almost identical, according to simulations. However, experimental spectra show that the intensity of the peak corresponding to (001) reflection (at 23.12º) is lower than the other two after the 400ºC-annealing, reaching a similar value after the 600ºC-annealing. A similar behaviour is reflected by the evolution of FWHM of (001) reflection in Fig. 3, as it only approaches the values of the other two peaks after a 700ºC-annealing.

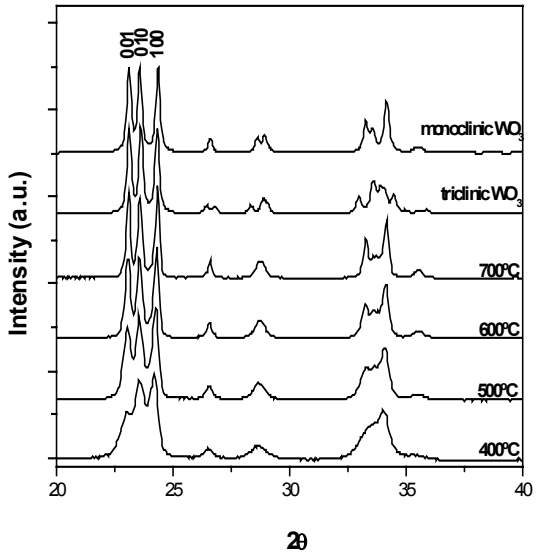

Fig. 2: *XRD spectra of obtained WO_3 (annealed at indicated temperature). Triclinic and monoclinic simulated spectra are also shown.*

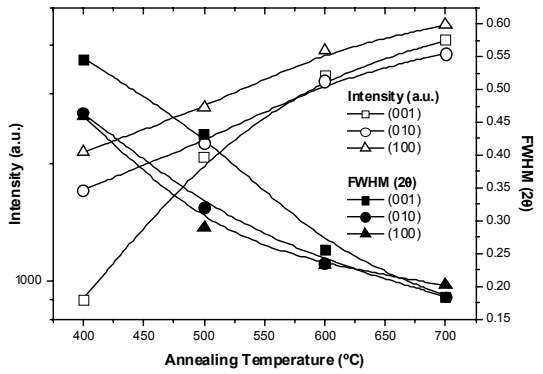

Fig. 3*: Evolution of FWHM and intensity of the three main XRD reflections with annealing temperature.*

Since gas sensors are usually operated at temperatures over room temperature, XRD spectra of 400ºC-annealed WO_3 were also acquired at higher temperatures (from room temperature to 300ºC) under laboratory atmosphere (Fig. 4). The purpose was to observe whether the

reflection (001) suffered any change when it was heated. As it is shown in Fig. 4, XRD patterns remain nearly identical and thus the source of this difference is present at least until 300ºC.

All in all, since these characteristics should be similar for these three reflections, either in the case of monoclinic or triclinic hypothesis, the nature of this difference should be attributed to the presence of some bulk defects that would mainly affect the (001) reflection peak. This defect would be present at normal sensor operating temperatures. This fact will be further discussed according to HR-TEM, SAED (Selected Area Electron Diffraction) observations and XRD simulations.

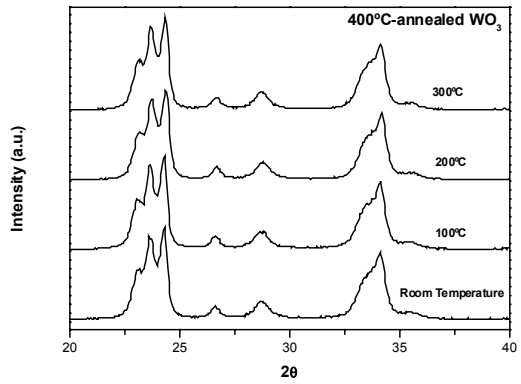

Fig. 4: *XRD spectra of 400ºC-annealed WO_3 acquired at different temperatures.*

Regarding crystalline structure identification by XRD, the distribution of diffraction peak intensities in the range 35-40º has been used in literature to distinguish between triclinic and monoclinic structures [5], as simulations of triclinic and monoclinic structures suggest in Fig. 2. In our case, intensities agree better with the hypothesis of a monoclinic structure. Nevertheless, due to the small mean crystallite size, reflections are badly resolved and the possibility of a mixture of both monoclinic and triclinic phases should be considered, as Raman investigations will show.

Annealing Temperature (ºC)	Crystallite size of WO_3 (nm)
400	27
500	37
600	53
700	68

Table 1: *Average crystallite size obtained from XRD data*

Using Scherrer's equation [6], average crystallite size of WO_3 was estimated from XRD spectra averaging results from the three main crystallographic directions, with an error

lower than 5 nm. Values for each annealing temperature are shown in Table 1. As it was expected, an increase in annealing temperature leads to grain growth. However, this value has to be taken as an estimation of the crystallite size average, whereas TEM investigations will provide a mean grain size average. In our case, crystallite size ranged from 27 nm for powder annealed at 400ºC to 68 nm for the one annealed at 700ºC (Table 1).

3.1.1.2 Raman spectroscopy

Fig. 5 presents a comparison of the Raman spectra of commercial tungstic acid and as-prepared WO_3. Tungstic acid has its main peaks at 806 and 710 cm^{-1}. These peaks are shifted to 812 and 700 cm^{-1} for the as-prepared WO_3. These bands are well identified as belonging to the stretching mode O-W-O, which in monocrystalline WO_3 are present at 807 and 715 cm^{-1} [7]. However, the peak at 947 cm^{-1}, that is present in commercial tungstic acid, has not completely disappeared in dried gel. This peak is reported to correspond to the mode W=O, which is also a bond of tungsten oxide hydrates ($WO_3 \cdot nH_2O$) when a water molecule occupies one axial position [7,8]. This confirms the XRD result about that some tungsten oxide hydrate was present. However, the presence of structural water should be taken into account as it has been reported to be present at this stage [2] and it could be the responsible for the shift in the Raman peaks due to lattice distortion. Alternatively, this vibration mode has been also attributed to terminal W=O bonds lying at the surface of microcrystalline grains of WO_3 [9]. Since grain size increases with annealing temperature, the intensity ratio of vibrations W=O/O-W-O is expected to decrease (O-W-O are bulk Raman active modes, responsible for the main vibrations at 715 and 807 cm^{-1} [7]). Therefore, it would be only detected in the case of small grain sizes.

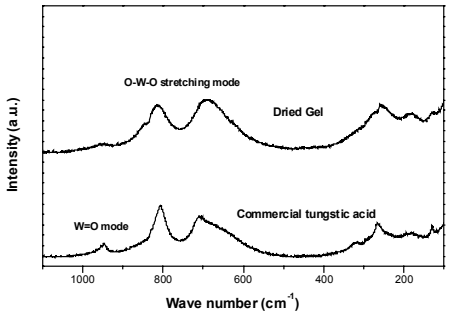

Fig. 5: *Comparison of the Raman spectra of commercial tungstic acid and dried gel obtained*

Raman spectra of annealed samples were also acquired. Fig. 6 displays the evolution of WO_3 nanocrystalline powders with annealing temperature. It can be seen that annealed WO_3 presents the typical structure of crystalline WO_3, with three main regions at 900-600, 400-200 and below 200 cm^{-1}. It has been established that they correspond, respectively, to stretching, bending and lattice modes. This great number of active modes is due to the distortion of the ReO_3-type structure in real monoclinic situation, as group theory shows that this structure should only have two active modes [10]. It has to be remarked that no trace of W=O bond was found. The disappearance of this 943 cm^{-1} vibration mode, under annealing, would imply a crystalline reorganisation and grain growth, as well as a dehydration process.

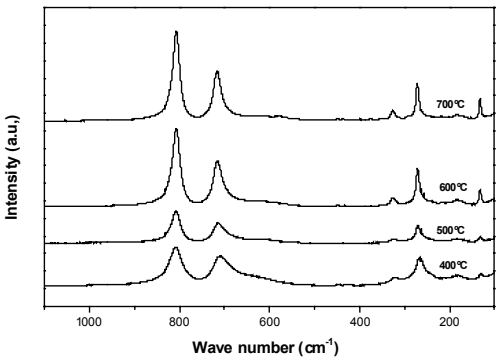

Fig. 6: *Evolution with annealing temperature of the Raman spectra of the sol-gel WO_3*

Raman spectroscopy is able to give a clear evidence of the monoclinic or triclinic nature of the WO_3 phase, since the lowest frequency phonon modes are different for both structures. Cazzanelli et al. [11] reported that monoclinic structure presents a peak at 34 cm^{-1}, while triclinic presents a peak at 43 cm^{-1}. Fig. 7 shows that only the peak corresponding to triclinic phase was present in powders annealed at 400º. When annealing temperature is increased, the peak at 34 cm^{-1} appears and both peaks seem to coexist in the range of annealing temperatures studied. Similar results concerning the evidence of triclinic-monoclinic coexistence in WO_3 by Raman have also been reported by Souza-Filho

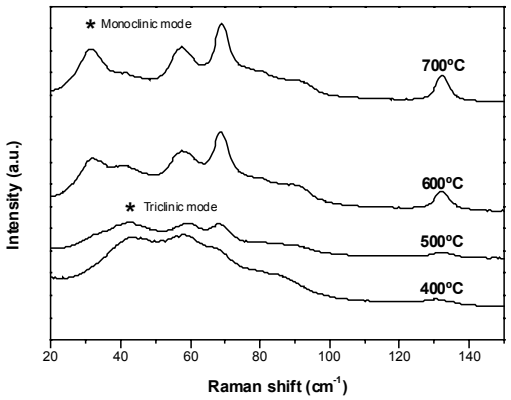

Fig. 7: *Low-frequency Raman spectra of obtained WO_3 (annealed at the indicated temperature).*

et al. [12]. Therefore, powders annealed at 400ºC have mainly a triclinic phase and both monoclinic and triclinic phases coexist at higher annealing temperatures.

as-prepared WO_3	annealed WO_3	vibration mode
953		ν(W=O)
810 689	807 715	ν(O-W-O)
261	380 330 280	δ(O-W-O)
	225	ν(W-O-W)
184 131 52	187 134 93 71 61 44 93	Lattice modes

Table 2: *Raman vibration modes found in as-prepared and annealed WO_3*

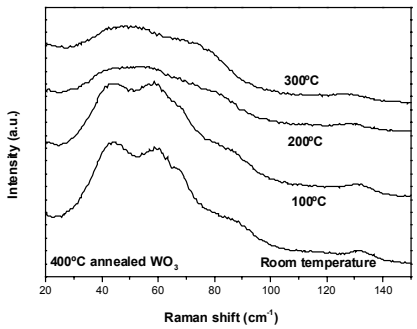

Fig. 8a: *Evolution of the low-frequency Raman spectra of 400ºC-annealed WO_3 with measurement temperature*

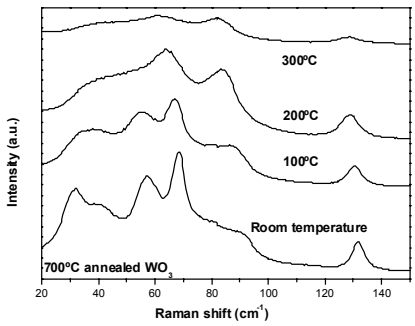

Fig. 8b: *Evolution of the low-frequency Raman spectra of 700ºC-annealed WO_3 with measurement temperature*

Raman spectra of 400ºC and 700ºC-annealed WO_3 were also acquired at different temperatures (from room temperature to 300ºC). The main target was to observe the evolution of the low frequency modes described previously. These results are shown in Fig. 8a and 8b. No trace of the 34 cm^{-1} monoclinic vibration was found on the 400ºC-annealed sample in the range of temperatures studied (fig. 8a). This fact is remarkable, since transition temperature between triclinic and monoclinic temperature is set around 20ºC [3].

In the case of 700ºC-annealed WO_3 (fig. 8b), 34 cm^{-1} monoclinic vibration became broader and collapsed over 100ºC with the peak at 43 cm^{-1}, typical of triclinic structure. Therefore, this would lead to think that 400ºC-annealed WO_3 is able to maintain its triclinic structure at least up to 100ºC. Over this temperature, unfortunately, it is not possible to determine the predominant crystalline structure since 700ºC-annealed WO_3 showed only a single broad peak over 100ºC. Similar situations have been already described for WO_3, such as a tetragonal metastable phase at room temperature [13], while it is considered to appear over 1000ºK.

3.1.1.3 X-ray photoelectron spectroscopy

Fig. 9 shows a survey scan, obtained in the 0-1100 eV range, of nanocrystalline WO_3 powder annealed at 500º for 5 hours. The material seems to be uncontaminated, since no spurious peaks belonging to foreign ions were found. Only carbon seems to be the prevailing adsorbed species. This carbon contamination is very usual and, in fact, it is often used to calibrate peaks position. Although there is no general agreement, a value of 484.8 eV is often assigned to this carbon peak of contamination.

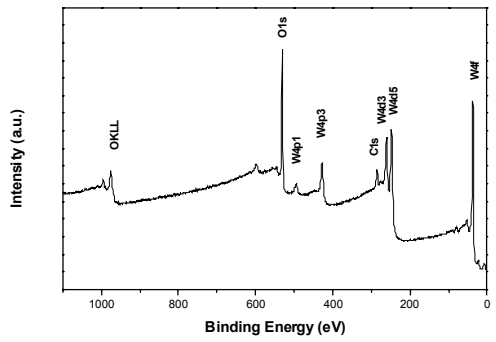

Fig. 9: *XPS survey scan of nanocrystalline WO_3 powder annealed at 500ºC.*

Fig. 10a and 10b show a typical fitting of the peaks corresponding to W 4f and O 1s regions respectively. The spectrum of the W 4f region shows a well-resolved double peak due to the $4f_{7/2}$ and $4f_{5/2}$ components (spin orbit splitting of 2.1 eV). On the other hand, the O 1s XPS band was deconvoluted in two components. The main peak was associated to the O^{2-} state, while the other one is assumed to come from a different source, probably coming either from rooted OH groups or from humidity in ambience.

Fig. 11a and 11b present detailed XPS scans of the W 4f and O 1s lines of the WO_3 samples annealed at different temperatures. Results from fittings (peak position and percentages) are shown in Table 2. From these results we can see firstly there are no significant differences

between powders annealed at different temperatures in any of the analysed features. The binding energy position of the W 4f doublet is typical of tungsten in the WO_3 phase [14-16]. The percentage of O^{2-} (calculated as the ratio of area corresponding to this fitting peak to the total O area) is around 70%, which agrees with other results concerning nanocrystalline metal oxides obtained by a similar chemical route. It is remarkable, though, the apparently low [O]/[W] surface ratio. Although it is well known that metal oxides usually present surface oxygen vacancies, it has to be considered this quantification by XPS may not be accurate enough. Such a low concentration of oxygen on the surface would lead to the formation of W^{4+} [17] and thus to the appearance of a new peak or a shoulder in the W 4f region, which is not observed in our case at all.

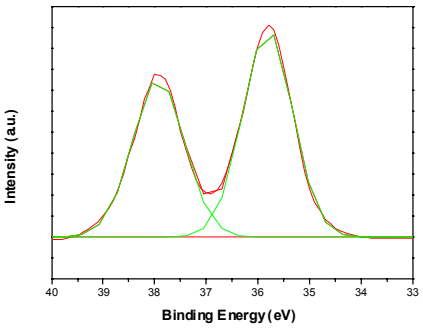

Fig. 10a: *Fitting of the W 4f band from the 700ºC-annealed WO_3*

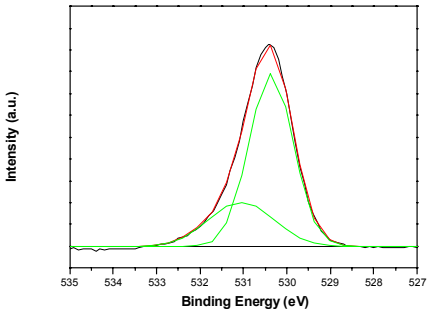

Fig. 10b: *Fitting of the O 1s band from the 700ºC-annealed WO_3*

Annealing temperature (ºC)	W 4f $_{7/2}$ (eV)	O 1s (eV)	O^{2-} percentage	[O]/[W]
400	35.9	530.5	70.6	2.55
500	35.7	530.4	70.5	2.55
600	35.9	530.5	69.2	2.58
700	35.8	530.5	72.9	2.59

Table 2: *XPS fitting results for nanocrystalline WO_3 annealed at different temperatures.*

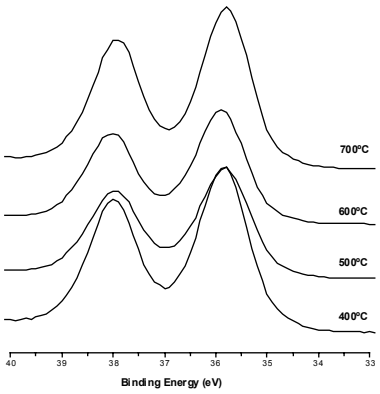

Fig. 11a: *Detailed XPS scans of W 4f lines for WO_3 nanocrystalline powder annealed at different temperatures*

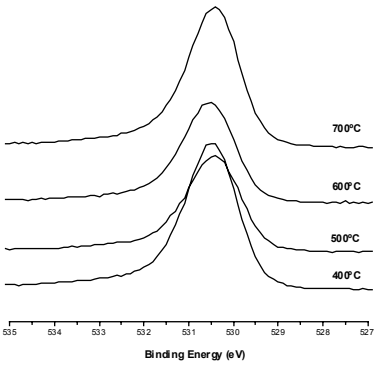

Fig. 11b: *Detailed XPS scans of O 1s lines for WO_3 nanocrystalline powder annealed at different temperatures*

3.1.1.3 Transmission electron microscopy

Grain size and shape was investigated by means of Transmission Electron Microscopy (TEM). The typical aspect of powder annealed at 400ºC and 700ºC are presented in fig. 12 and 13, where a general bright field TEM view is shown. Counting statistics after simple visual inspection are also presented.

These figures indicate that 400ºC-annealed WO_3 powder presents a very irregular shape, although the distribution of size is rather narrow around 16nm. On the other hand, 700ºC-annealed powder has a more faceted and homogeneous shape. Besides, the increase in annealing temperature not only produces an obvious increase in grain size (up to 120 nm) but it also produces a large broadening of the size distribution.

Fig. 14 and 15 show the Transmission Electron Diffraction Patterns corresponding to 400ºC and 700ºC-annealed WO_3, respectively. Corresponding plane spacing, and thus material composition, can be deduced from the diameter of the rings (Tables 4 and 5). They have been mainly identified with WO_3 in monoclinic or triclinic structure (as in the XRD case, it is not possible to distinguish these two structures when dealing with nanocrystalline WO_3). Non-identified spacings have been labelled as A and B.

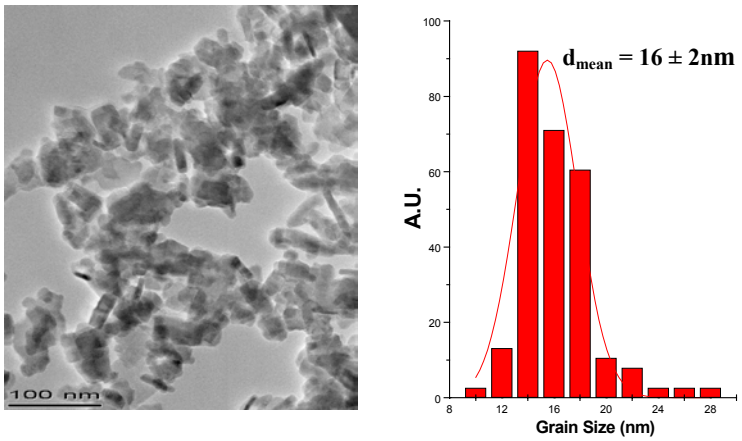

Fig. 12: *General TEM view of the 400ºC-annealed WO_3 powder and the respective grain size histogram.*

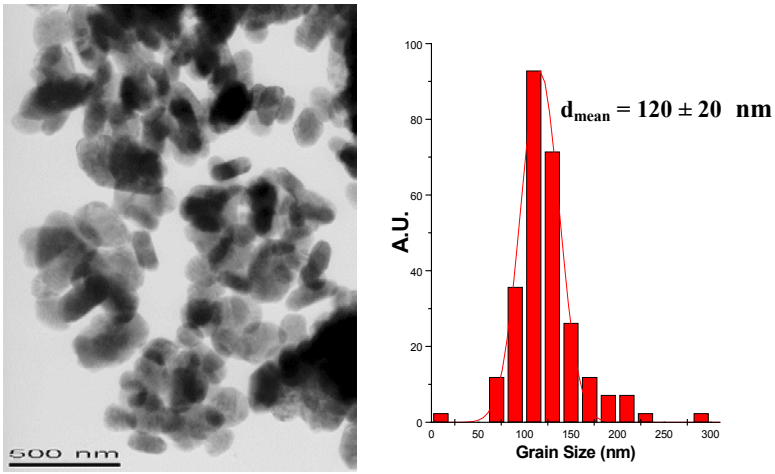

Fig. 13: *General TEM view of 700ºC-annealed WO_3 powder and the respective grain size histogram.*

Concerning crystalline defects, a detailed analysis performed by high-resolution electron microscopy (HRTEM) showed some wide fringes next to the borders of some of the 400ºC annealed WO_3 nanoparticles, as it is marked with black arrows in figure 16. Detailed Selected Area Electron Diffraction (SAED) pattern showed large reflections corresponding to typical WO_3 and short reflections that have been assigned to Magneli phases (SAED pattern inset in fig.16). These phases correspond to oxygen deficient tungsten trioxide with formulas W_nO_{3n-2} [18]. Since these wide fringes were superposed to the WO_3 atomic

planes, a detailed digital image analysis was carried out in order to separate these phases and study them. Firstly, a representative squared area from Fig. 16 was selected (Fig. 17a) and a FFT image of this squared region was obtained (fig. 17b). Afterwards, spots corresponding to the WO_3 planes and to the Magneli Phase on the FFT were selected and filtered by using a mask filter, in order to obtain their representation in separate images, as shown in fig. 17c and 17d. From these images, it can be concluded that the wide planes observed correspond to shear planes, in good agreement with those $\{103\}_R$ crystallographic shear (CS) defects observed by J. Sloan et al. in [19], where $\{103\}_R$ refer to the family of equivalent directions expressed in the ideal ReO_3 cubic cell. Visible between the CS planes, 0.38 nm lattice fringes corresponding to the (010) WO_3 planes were found.

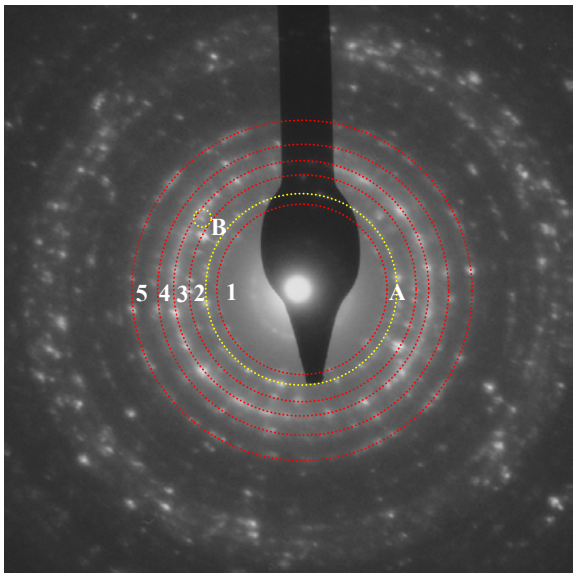

Fig. 14: *SAED pattern corresponding to 400ºC-annealed WO_3. Diffraction rings and spots show the coexistence of WO_3 (1-5) and another undetermined phase (A-B), although it is in low proportion*

#Ring	d (Å)	planes	Phase	#Spot	d (Å)	planes	Phase
1	5.23	{0-11}	WO_3	A	4.43		??
2	3.84	{100}	WO_3	B	3.54		??
3	3.34	{021}	WO_3				
4	3.08	{111}	WO_3				
5	2.52	{12-1}	WO_3				

Table 3. *SAED pattern profile indexation corresponding to that shown in figure 14*

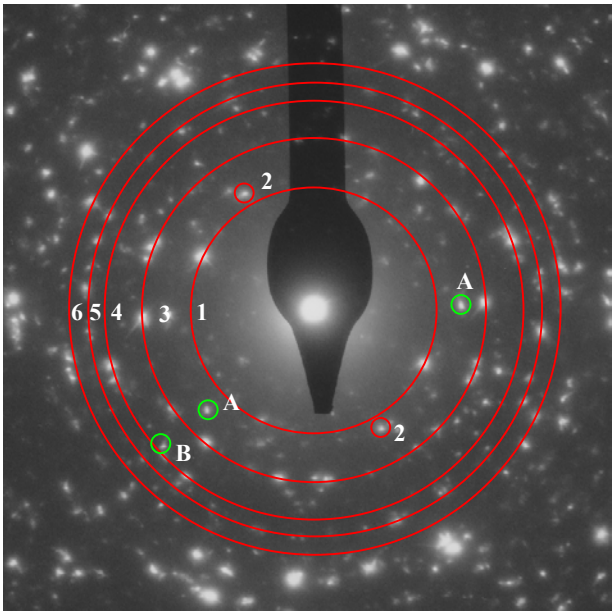

Fig. 15: *SAED pattern corresponding to 700ºC-annealed WO_3. Diffraction rings and spots show the coexistence of WO_3 (1-5) and another undetermined phase (A-B), although it is in low proportion*

#Ring	d (Å)	planes	Phase	#Spot	d (Å)	planes	Phase
1	3.76	{020}	WO_3	A	3.16		??
2	3.42	{110}	WO_3	B	2.23		??
3	2.66	{10-2}	WO_3				
4	2.17	{12-2}	WO_3				
5	2.01	{131}	WO_3				
6	1.86	{210}	WO_3				

Table 4. *SAED pattern profile indexation corresponding to that shown in figure 14b*

In tungsten trioxide, it is possible to shear the structure in such a way that oxygen vacancies are eliminated and some tungsten atoms remain more closely spaced, so pairs of W^{5+} atoms are found in order to compensate the charge left by the oxygen deficiency. These phases, called Magneli phases, correspond to oxygen deficient tungsten trioxide. All of them present a crystalline structure based on WO_3 zones (corner sharing WO_6 octahedra) linked by units of edge sharing octahedra in the CS phases [19]. These bulk defects influence the electrical transport properties: carrier concentration increases, as each missing oxygen atom contributes two carriers, and carrier mobility decreases [20]. This kind of defect was not found by HRTEM in samples annealed at temperatures over 400ºC.

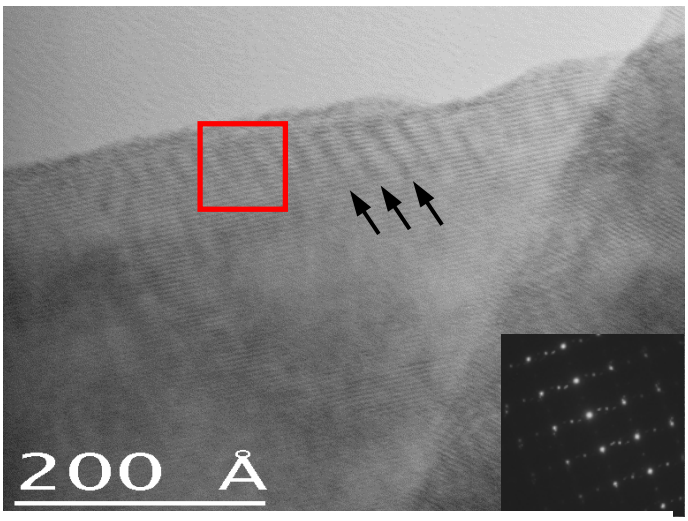

Fig. 16: *HRTEM micrograph from a 400ºC annealed WO_3 nanoparticle. The inset corresponds to the SAED pattern of this nanoparticle. Wide fringes have been marked with black arrows. The squared region has been digitally analyzed in figure 17.*

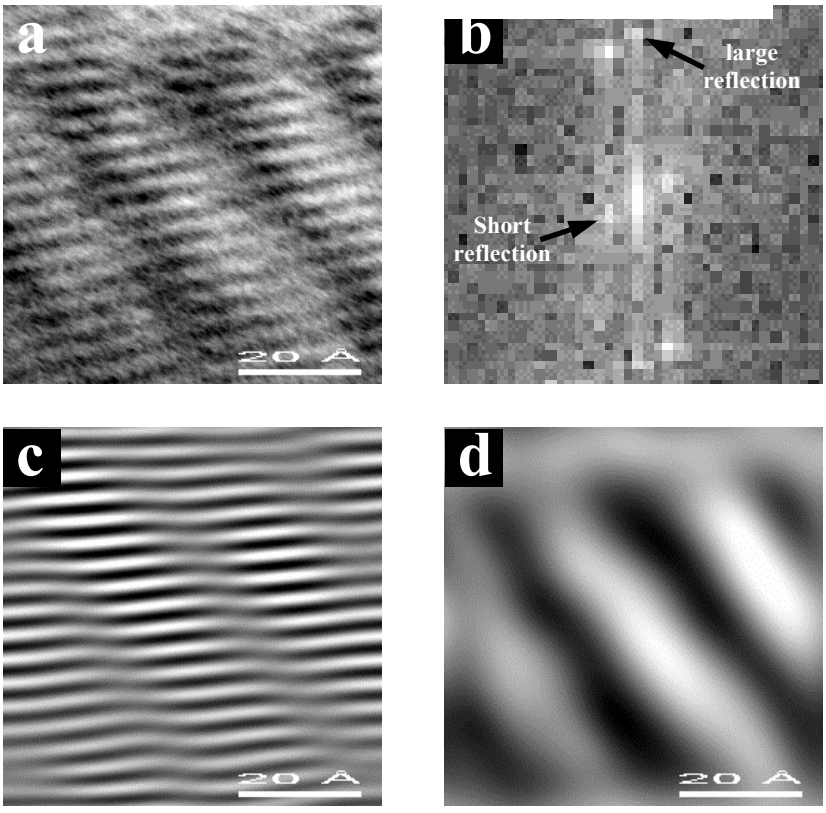

Fig. 17: a) *Magnified detail of the squared region in figure 16.* ***b)*** *FFT of a).* ***c)*** *0.38 nm WO_3 lattice fringes corresponding to the $\{100\}_R$ planes obtained after selecting the large reflections in b).* ***d)*** *$\{103\}_R$ crystallographic shear (CS) defects from Magneli phases obtained after selecting the short reflections in b).*

3.1.1.4 Diffuse reflectance infrared spectroscopy

Fig. 18 displays the DRIFT infrared spectra of the nanocrystalline WO_3 as prepared and after annealing at 400ºC and 700ºC. These spectra were recorded after evacuation at room temperature and the samples were not previously degassed. Three different regions will be differentiated: under 1000 cm^{-1}, between 1000 cm^{-1} and 3000 cm^{-1} and from 3000 cm^{-1} on.

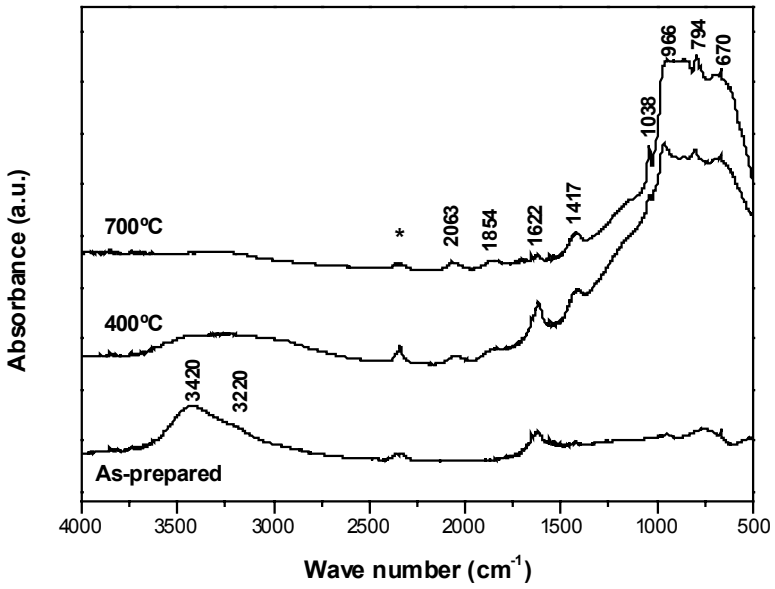

Fig. 18: *Infrared diffuse reflectance spectra of as-prepared, 400ºC-annealed and 700ºC-annealed. All spectra were recorded after evacuation at room temperature. (Symbol * marks atmospheric CO_2 traces).*

Vibrations at 670 cm^{-1} and 790 cm^{-1} are well reported to be due to lattice vibrations ν (O-W-O) [1]. These vibration modes are visible in annealed samples, while as-prepared WO_3 presents a broader signal in this region. These modes are related to those found by Raman spectroscopy at 715 and 807 cm^{-1}. The third bound at 966 cm^{-1} may have a different nature in as-prepared than in annealed WO_3. It has been reported to be due to W=O bonds in $WO_3 \cdot nH_2O$ [1] and so it could be identified. One axial position would be occupied by a water molecule, so the corresponding W-OH_2 bond would be rather long (~2.3 Å) whereas the opposite axial bond is short (~1.7 Å), giving to this terminal bond a double-bond character (W=O). On the other hand, in the case of annealed WO_3, it has been identified as a vibration coming from a shorter W-O bound, probably near the surface of the grain [21].

All in all, both represent a shorter tungsten-oxygen bound, although their source is different.

In the second region, a peak at 1038 cm^{-1} is found in both annealed samples. This mode is undoubtedly related to W=O vibrations. Since these samples have been annealed, and thus their content of water must be low, this vibration can not come from W=O stretching vibrations, but from surface W=O species [21,22]. Vibration mode at 1417 cm^{-1} has been attributed to a stretching vibration of OH groups [1,23], while 1622 cm^{-1} vibration comes from a bending mode of adsorbed H_2O [24]. Finally 1854 cm^{-1} and 2063 cm^{-1} vibrations are due to overtones or combinations of lower frequency vibrations [21,25,26]. The band near 1870 cm^{-1} might correspond to the first overtone of the absorption detected around 966 cm^{-1}, and the band at 2070 cm^{-1} can be assigned to the first overtone of the weak band observed at 1038 cm^{-1}.

Finally, the broad band present between 3500 and 3000 cm^{-1} is due to hydrogen bounded hydroxyl groups [24]. It is remarkable how this band decreases with annealing temperature and that it is still present after the 400ºC-annealing. More specifically, 3420 cm^{-1} vibration has been attributed to the OH stretching mode of adsorbed water, whereas 3220 cm^{-1} vibration is probably due to hydrogen bounded WOH groups.

Wave number (cm^{-1})	Vibration mode	Reference
670 790	ν(O-W-O)	[1]
966	short ν(W-O)	[21]
1038	terminal ν(W=O)	[21,22]
1417	δ(OH) from OH groups	[1,23]
1622	δ(OH) from H_2O	[1,24]
1854	2ν(W-O)	[21]
2063	2ν(W=O)	[21,25,26]
3000-3500	ν(OH)	[1]
3220	ν(OH) from OH groups	[1,24]
3420	ν(OH) from H_2O	[1,24]

Table 4: *Infrared vibration modes found in WO_3*

3.1.2 Discussion and conclusions

Crystalline structure

According to XRD and Raman results, as-prepared WO_3 presents broad reflections and vibrations modes typical of crystalline WO_3. The broadening is undoubtedly due to the low crystallite size, as well as to the possible presence of crystal defects. However, some traces of W=O vibrations and low intense XRD peaks at $2\theta=16.5º$ and $2\theta=25.6º$ are showing that some water is present in this samples. This point is clearly confirmed by infrared studies, which displayed a great adsorption in the 3000 cm^{-1} region. Therefore, as-prepared WO_3 should be identified as poorly crystalline WO_3 with some water content, either as structural water or as $WO_3 \cdot nH_2O$.

Annealing treatments revealed that 400ºC was a suitable temperature to obtain crystalline WO_3. Some previous studies had already confirmed that temperatures over 350ºC degrees are necessary in order to obtain crystalline WO_3 [27,28]. This annealing treatment implies a progressive disappearance of crystal defects, leading to a higher degree of crystallinity in the solid, and an increase in the particle size as the annealing temperature is raised (confirmed by TEM investigations).

XRD and SAED patterns were not able to determine, however, if the crystalline structure was monoclinic or triclinic. These structures present very similar diffraction patterns and, when dealing with nanocrystalline samples, it is not possible to determine the difference with diffraction techniques. Fortunately, Raman investigations showed a clearer answer to this question. It was found that 400ºC-annealed WO_3 powder had mainly a triclinic structure. As annealing temperature increased, vibration lattice mode corresponding to monoclinic structure appeared. Therefore, a coexistence of both phases was found when annealing temperature ranged between 500-700ºC. This is in agreement with those studies that show these two crystalline structures can be present at room temperature in crystalline WO_3.

Finally, it must be pointed out that Raman investigations showed that triclinic structure was present in 400ºC-annealed WO_3 even when it was heated at temperatures up to 100ºC. This is remarkable since transition temperature between triclinic and monoclinic structures has been fixed at 17ºC at atmospheric pressures. Over 100ºC it was not possible to determine if triclinic structure was still stable due to the broadening of peaks.

Crystalline defects - Shear planes

XRD spectra showed an anomalous difference between the three main reflections present in 400ºC-annealed WO_3, as the (001) reflection presents a wider and not so well resolved reflection than the other two reflections, (010) and (100). As annealing temperature increased, this difference diminished until all three reflections had similar features after the 700ºC-annealing.

Furthermore, TEM investigations revealed that only 400ºC-annealed WO_3 presented crystallographic shear defects. These kinds of defects are related to the appearance of oxygen vacancies in the lattice. Fig. 19 shows the lattice structure of pseudocubic (monoclinic or triclinic WO_3). Tungsten atoms are located in the centre of the octahedra formed by oxygen atoms (as explained in chapter 1), so they are bounded to four oxygen atoms of the plane showed here. When oxygen vacancies (black dots in Fig. 19, left-hand) occur in some directions, called shear planes, the structure is able to shear in such a way that vacancies are eliminated (right-hand). These shear planes are typically [1k0] directions in the case of WO_3. More details about these structures can be found in ref. [18].

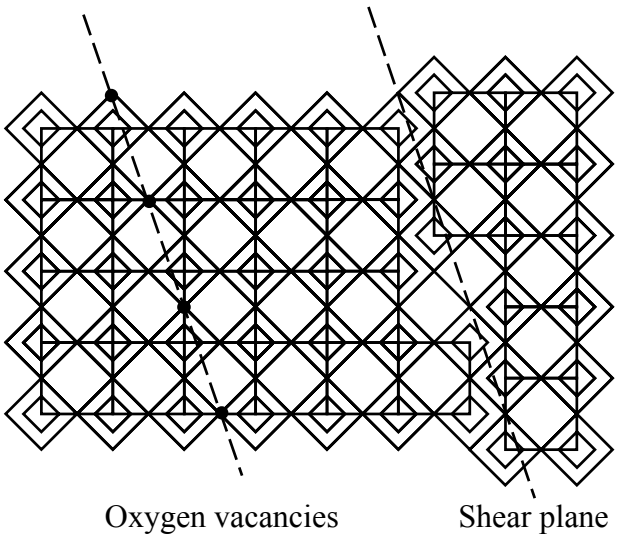

Fig. 19: *Typical shear plane representation of a WO_3 structure*

Although these substoichiometric regions seemed to be very localised, as observed diffraction patterns were those of typical stoichiometric WO_3, it is reasonable to think that some shear planes could be also present inside the bulk material. These planes may affect the intensities of XRD reflections and this effect has been studied by XRD simulations with the software Diffax [29]. Two kinds of layers were defined: the first one corresponds to an unfaulted WO_3 derived structure (cell nº 1), whereas the other one (cell nº 2) corresponds to the planar defect. Both cells are represented in Fig. 20, where vectors defining the unit cell 1, 2 and cubic unit cell are also shown. In this representation, W atoms occupy the centre of oxygen octahedra. For the sake of simplicity, the atomic positions have been first described in a cubic representation, the unit cells being artificially distorted at the end (orthorhombic unit cells) to reflect the distortion of WO_3 structure. The cells parameters used for the pseudo-cubic unit cell were a_0 = 0.365 nm, b_0 = 0.377 nm, c_0 = 0.384 nm and the shear plane direction was [013], according to HRTEM investigations.

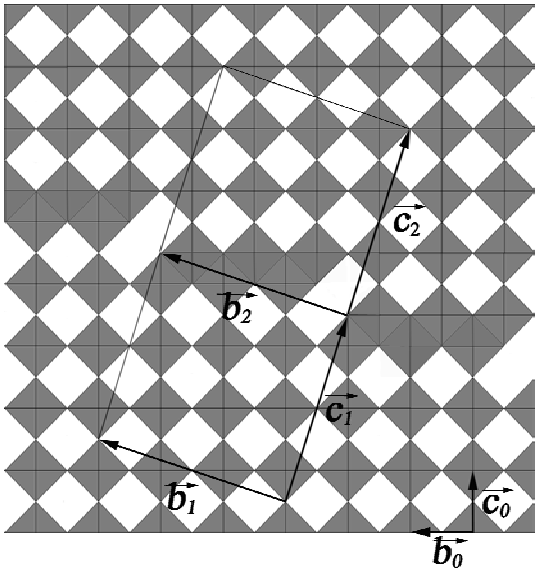

Fig. 20: *Representation of the layers usedfor XRD simulation: the first one corresponds to an unfaulted WO_3 derived structure (cell nº 1), whereas the other one (cell nº 2) corresponds to the planar defect.*

Simulations have been performed supposing a random stacking of layer 1 and layer 2 with a given probability associated to each layer. On figure 21, simulations for different probabilities of shear planes are shown. It can be seen that for a zero percent probability for layer 2, i.e. a stacking of unfaulted WO_3 layers, the distribution of intensities for the three main diffraction peaks remain similar to that observed for monoclinic or triclinic structures, confirming the validity of

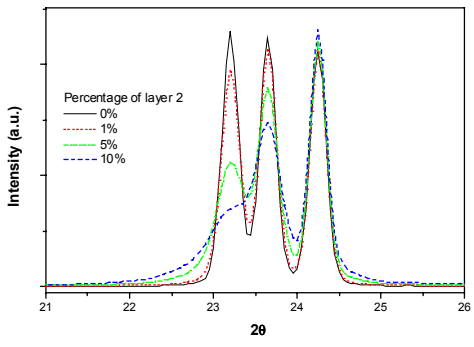

Fig. 21: *XRD simulations considering different probabilities of shear planes.*

the approximation done on atomic positions. When the probability of layer 2 presence increase, the intensities of calculated (001) reflection diminishes while its width increases. A similar tendency is observed for the (010) reflection but to a lower extent. These results agree with the evolution of experimental XRD diffraction patterns of samples annealed between 400°C and 700°C (fig. 3), confirming that the TEM observed CS planes could be responsible for the anomalous XRD pattern of the (001) reflection after a 400ºC-annealing. Therefore, this anomalous reflection behaviour can be used as an indirect proof of the presence of bulk oxygen deficiencies. Higher annealing temperatures would reduce the presence of these defects, according to experimental a simulated XRD patterns and TEM observations.

To sum up, the main conclusions that can be drawn from the characterisation of pure WO_3 are obtained from tungstic acid are:

- As-prepared WO_3 is formed by WO_3 and WO_3:nH_2O.
- After annealing at temperatures between 400ºC and 700ºC, crystalline WO_3 is obtained. Crystallite size is between 27 and 68 nm (obtained by XRD) and grain size is between 15 nm and 120 nm (obtained by TEM). These values suggest that, at low annealing temperatures, the estimation of the crystallite size is probably affected by the presence of defects that make increase its value. On the other hand, t higher annealing temperatures, each grain may have more than one domain with different orientation, making grain size nearly twice bigger than crystallite size.
- Crystalline structure of 400ºC-annealed WO_3 was mainly triclinic, as revealed by Raman spectroscopy. As annealing temperature increased, monoclinic structure appeared, leading to coexistence of both structures in 700ºC-annealed WO_3. These structures were stable
- Crystalline shear planes appeared in 400ºC-annealed WO_3, according to TEM investigations. XRD simulations were performed in order to include this defect and fit experimental XRD spectra. These simulations allowed us to follow the evolution of the concentration of these defects, revealing that they disappear after the 700ºC-annealing. High-temperature XRD spectra indicated that these defects are stable in 400ºC-annealed WO_3 up to 300ºC.
- The presence of surface terminal oxygen ions bonded to tungsten atom through W=O bond in annealed WO_3 was confirmed by DRFITS spectra.

3.2 Catalysed nanocrystalline WO_3 powder

3.2.1 Copper catalysed WO_3

3.2.1.1 Results

As already noted in Chapter 2, copper was introduced in different concentrations (0.2, 1, 2 and 5 atomic percentages) and the as-obtained powders were annealed at two different temperatures (400ºC and 700ºC). Firstly, bulk properties of copper catalysed WO_3 powders were analysed by XRD and Raman spectroscopy. XRD spectra displayed neither significant differences between differently catalysed samples on WO_3 diffraction peaks, nor any peak corresponding to a copper phase.

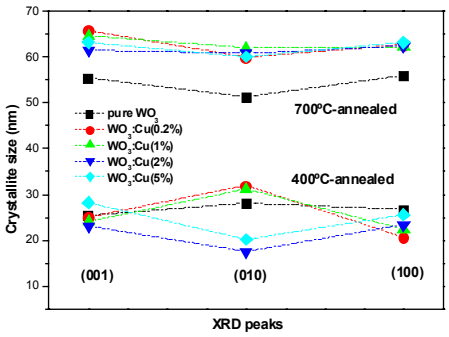

Fig 22: *Crystallite size of WO_3:Cu powders obtained from the three main crystallographic directions.*

As already mentioned, average crystallite size of WO_3 powders can be estimated from XRD spectra using Scherrer's equation. Results from the three main crystallographic directions were calculated and they are displayed in Fig. 22. It is evident from this figure that the different concentrations of copper do not have a significant effect on the crystallite size of the powders. Moreover, the crystallite size remains similar to that of pure WO_3 after the 400ºC-annealing, whereas copper-catalysed WO_3 has a slightly higher crystallite size after the 700ºC annealing.

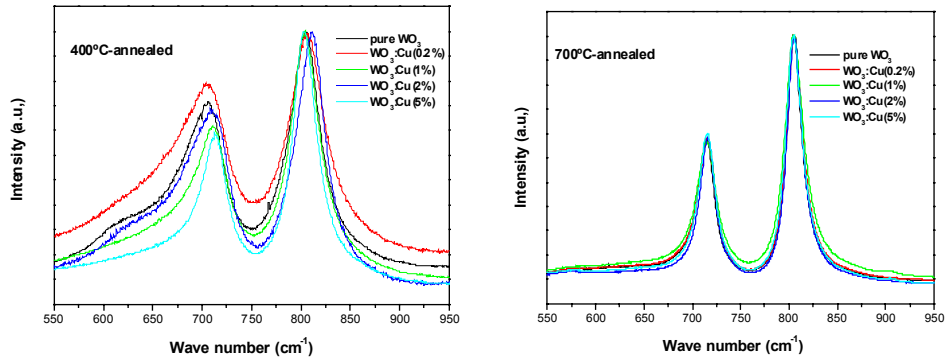

Fig. 23: *Selected region of the Raman spectra of 400ºC-annealed (left-hand) and 700ºC-annealed (right-hand) WO_3:Cu powders.*

Fig. 23 displays a selected region of the Raman spectra of pure and copper-catalysed WO_3. These spectra have been normalised to the maximum intensity of the 807 cm^{-1} vibration mode (which is usually the most intense vibration mode). This comparison reveal that, while 700ºC-annealed materials present virtually identical vibrations, 400ºC-annealed powders present different relative intensities of the two peaks, peak shifts and different peak shapes (i.e. different full width at half maximum or FWHM). This is illustrated in Fig. 24, where the FWHM of the 807 cm^{-1} Raman vibration of 700ºC-annealed WO_3:Cu is presented as a function of nominal copper content. This figure clearly indicates that the FWHM of the peak is highly dependent on copper content, reducing its value as copper content increases.

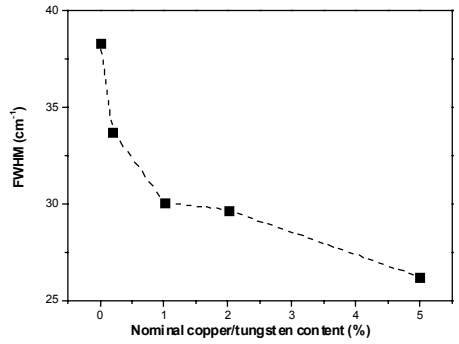

Fig. 24: *Evolution of the FWHM of the 807 cm^{-1}Raman vibration with nominal copper content in 700ºC-annealed WO_3:Cu*

The chemical state of copper centres was studied by means of XPS. No copper traces were founded in WO_3:Cu(0.2%) by this technique, being only detected for nominal concentrations over 1%. Oxidation states of copper supported on catalysts, a similar case to the one we deal with, have been usually assigned using the $Cu2p_{3/2}$ binding energy and its associated shake-up satellite (if present) [30]. As a matter of fact, the Cu $2p_{1/2}$peak is also detectable, although it has a lower intensity. Fig. 25 displays these two peaks in 400ºC annealed copper-catalysed WO_3. The first interesting feature this figure reveals is that there is not a satellite peak around 943 eV. This satellite peak is a typical characteristic of

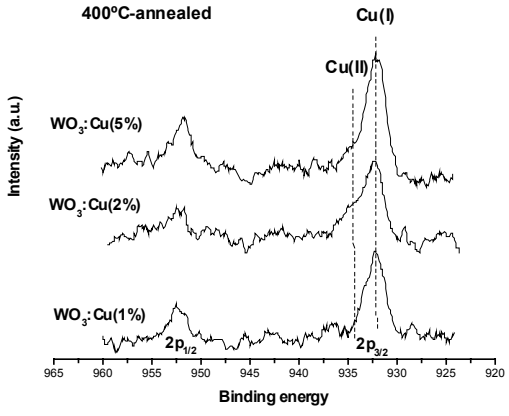

Fig 25: *XPS spectra showing the Cu $2p_{3/2}$ region for 400ºC annealed WO_3:Cu.*

Cu(II), what clarifies that our Cu signal is probably mainly due to a more reduced copper species. The peak $Cu2p_{3/2}$ was deconvoluted using two peaks, accordingly with literature [30-32]. Binding energies and percentages from the total copper signal corresponding to both peaks, as well as the total Cu/W percentage are displayed in Table 9. From these data it is clear that there is an intense component with binding energy between 932.2 and 932.5 eV and a second one around 933.9-934.2 eV. The first of these peaks is characteristic of reduced copper, either Cu(I) or metallic copper, since some authors claim that by XPS it is not possible to fully determine the difference in binding energy between these two species, while other authors do assign this position to Cu(I). Nevertheless, this peak will be labelled as Cu(I), taking into account that the sample was stored in ambient air before XPS measurements and that dispersed metallic copper is easily oxidised under these conditions [32]. On the other hand, the assignment of the less intense component to Cu(II) is fully supported by literature.

		Cu(I) BE (eV)	*Cu(II) BE (eV)*	*Cu(I) %*	*Cu(II) %*	*Cu/W*
WO_3:Cu(1%)	**400ºC**	932.5	934.2	85	15	0.008
	700ºC	932.3	934.2	89	11	0.009
WO_3:Cu(2%)	**400ºC**	932.3	934.0	71	29	0.011
	700ºC	932.3	933.9	69	31	0.012
WO_3:Cu(5%)	**400ºC**	932.2	934.4	87	13	0.017
	700ºC	932.4	934.0	63	37	0.014

Table 9: *Results of peak deconvolution of the copper photoelectron signal after calcination*

These data reveal there is not an evident correlation between the content of Cu(I)-Cu(II) and the annealing temperature or chromium content. Only WO_3:Cu(5%) shows a clear oxidation of Cu(I) to Cu(II) as annealing temperature increases from 400ºC to 700ºC.

Another interesting point to notice is the Cu/W ratio. It is evident that copper concentration on the surface of WO_3 is lower than the nominal content and it has a low increase with nominal concentration. There can be two possible explanations for these phenomena. One is that the impregnation method used is not efficient enough and most of the copper is lost in the evaporation of the precursors and/or the annealing process. The second reason may be that copper has been able to diffuse inside the structure of tungsten oxide and thus it can not be detected by XPS, being this technique mainly superficial. Moreover, according to the

Cu/W ratio, data suggest that copper content slightly increases when annealing temperature increases (but in the 5% nominal copper content). If the number of copper centres were the same after the 400ºC and 700ºC, and provided there were no diffusion to the bulk, the superficial Cu/W ratio should increase, as there is an evident grain growth reported above. This point will be further discussed in the *discussion* subsection.

In order to study with further detail the chemical state of copper centres, selected samples were analysed by EPR (WO_3:Cu(0.2%) and WO_3:Cu(2%)). As explained in Chapter 2, as prepared powders were annealed at 400ºC and 700ºC (synthetic air) in a quartz apparatus suitable for both gas-flow and EPR measurements, so as to avoid contact with uncontrolled atmosphere. Cu^{2+} ions are $3d^9$ paramagnetic ions and thus observable by EPR. On the contrary, Cu^{1+} ions are dimagnetic ($3d^{10}$) and so EPR silent.

The spectrum of the as-prepared WO_3:Cu(0.2 %) sample showed well resolved resonance lines of magnetically diluted Cu (II) centres (species A), with $g_{\parallel} = 2.397$, $g_{\perp} = 2.073$ and $A_{\parallel} = 100.1$ G (Fig. 26). This spin-Hamiltonian parameters correspond to an axial structure ($g_{xx}=g_{yy}= g_{\perp}$;$g_{zz}= g_{\parallel}$). The g values are higher than the free spin value (g_e=2.0023) and the hyperfine coupling tensor, due to the I=3/2 nuclear spin of ^{63}Cu and ^{65}Cu which splits each resonance in four lines, has the structure $A_{\parallel} > A_{\perp}$. The magnetic tensor values found here are consistent with those of bivalent copper in a tetragonal symmetry field of oxygen atoms [33].

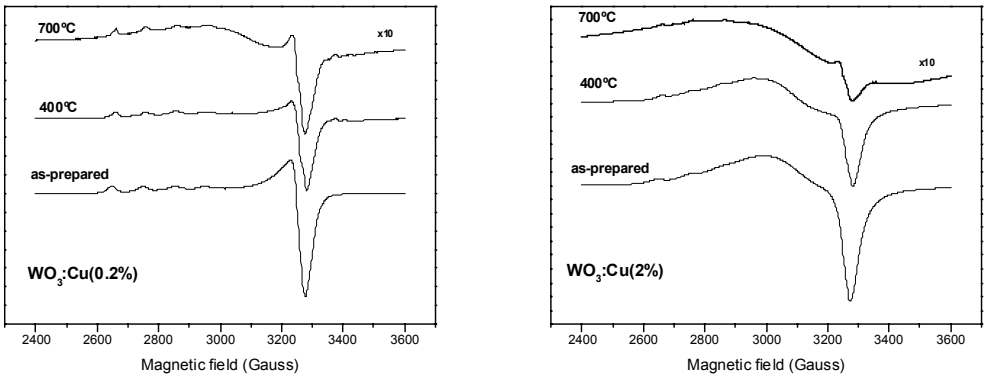

Fig. 26: *EPR spectra, recorded at 123 K, of WO_3:Cu(0.2%) (left-hand) and WO_3:Cu(2%) (right-hand).*

After the annealing at 400°C and 700°C (Fig. 26), the spectrum of WO_3:Cu(0.2 %) resulted from the overlap of two different signals, species B and C. The signals of the species B were attributable to magnetically isolated Cu(II) centres with $g_{\parallel} = 2.399$, $g_{\perp} = 2.073$ and $A_{\parallel} = 97.7$ G, values slightly different from those of species A. On the other hand, species C presents an unresolved broad resonance centred at g = 2.142 is due to magnetically coupled Cu(II) centres [34]. The C:B intensity ratio increased with the annealing temperature.

As in the previous case, WO_3:Cu(2 %) sample showed the EPR signals of A species in the as-prepared sample and of B species, in samples annealed at 400 and 700 °C (Fig. 26). By contrast, C species was already present in the as-prepared powders. Moreover, the C/B intensity ratio was higher in WO_3: Cu(2%) samples than in WO_3: Cu(0.2%) after the same annealing treatments.

The main parameters obtained from simulations that fitted EPR measurements are summarised in Table 10.

Species	$g_{\parallel}$	$g_{\perp}$	$A_{\parallel}$
A	2.397	2.073	100.1
B	2.399	2.073	97.7
C	2.142	2.142	-

Table 10: *EPR parameters of WO_3:Cu obtained from simulations.*

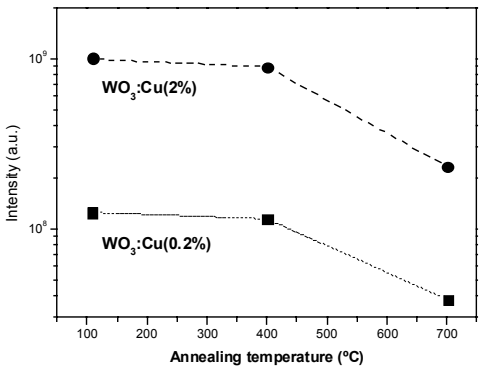

Fig. 27: *Evolution of the Cu(II) EPR-abundance with annealing temperature.*

As explained in chapter 2, EPR spectra can also give us quantitative information by double integration of the signal. Results are displayed in Fig. 27. Firstly, in the as-prepared samples (labelled here as annealed at 110ºC), the amount of Cu(II) centres in WO_3:Cu(2%) is around ten times that of WO_3:Cu(0.2%). Interestingly, there is a clear decrease of the intensity as annealing temperature increases from 400ºC to 700ºC, similar

in proportion for both materials. Although this would apparently imply a reduction of Cu(II) to Cu(I), which is EPR silent, it has been reported that, under certain conditions, Cu(II) EPR-silent centres are also possible [35]. This point will be further discussed in the next subsection.

Finally, it must be pointed out that copper-catalysed WO_3 was also studied by TEM and no cluster of copper was found. Besides, EELS was not able to obtain a distinct signal of copper, probably due to its low concentration on the surface of WO_3.

3.2.1.2 Discussion

As revealed by XPS, copper content on WO_3 is much lower than the nominal load and it has a low growth with increasing nominal content. Actually, if all nominal copper were well distributed onto the surface of WO_3, XPS should have revealed a higher Cu/W ration then the nominal, since it was calculated taking into account all the tungsten atoms and XPS is mainly superficial. This is a very common effect and the main reasons to explain this phenomena are: loss of the additive (copper) during the impregnation-drying-annealing treatment, diffusion of the additive to the bulk of WO_3 (XPS silent) and formation of clusters on the surface of particles (bulk atoms of the additive cluster would be XPS silent).

XRD revealed that no copper phase was intense enough to be detected and that diffraction peaks of bulk WO_3 were not affected by copper addition. Besides, no sign of cluster formation was detected by TEM investigations. Furthermore, only 400ºC-annealed Raman spectra were apparently dependent on copper content, whereas 700ºC-annealed ones were virtually unaffected. These evidences suggest that most of the copper must be superficial and that, if has diffused inside the bulk, it is either dispersed or its quantity can not be really significant. Since no clusters of copper were detected by TEM-EELS, it seems reasonable to assume that the efficiency of the impregnation method was not as good as expected. Nevertheless, EPR data indicate that in WO_3:Cu(0.2%) at least some Cu^{2+} is present, being under the detection limit of XPS.

Furthermore, EPR spectra of as-prepared WO_3:Cu(0.2%) presents a single contribution from A species, what clearly indicates that Cu(II) are well dispersed on WO_3. As annealing temperature increases to 400ºC, the amount of Cu(II) species remain nearly constant. A similar situation is found in WO_3:Cu(2%), what indicates that copper is lost in the impregnation-drying step.

Finally, it is interesting to comment the apparent diminution of Cu(II) content suggested by EPR data after the 700ºC-annealing and not detected by XPS. Similar effects has been already described and it was suggested that, although reduction of Cu(II) to a lower oxidation state was possible, the formation of Cu(II) species that are EPR silent can not be ruled out. As regards WO_3:Cu(0.2%), it could be hypothesised that Cu(II) ions were well dispersed in the amorphous and hydrated framework of the as-prepared WO_3. During annealing treatment, the removal of residual solvent molecules, the condensation of hydroxo groups in the hydrated WO_3 and the formation of the crystalline WO_3 phase, caused densification of the structure and the copper ions approached. As a result, spin coupling effects became active among Cu(II) ions, which interacted via oxo-bridges in crystalline WO_3, as revealed by the appearance of species C. However, as annealing temperature increases to 700ºC, the diminution of Cu(II) would imply a reduction to Cu(I), probably due to dehydration. This process agrees with the change of oxidation state that frequently occurs in copper complexes when the number of co-ordinated ligands decreases from 6 to 4 [36]. Besides, it has been reported that during the dehydroxylation of Cu(II)

$$Cu^{2+}OH^{-} \leftrightarrow Cu^{+} + OH^{*} \qquad (1)$$

doped-zirconia catalysts prepared by sol gel method, Cu(II) centres were reduced to Cu(I) and these latter centres were stable against successive re-oxidation [35]. A proposed path for this reaction is:

where OH^{*} is an hydroxyl radical.

However, it is possible that this process leads to the formation of Cu(II) centres that are actually EPR silent, as indicated by Hall et al[37]:

$$2\left[Cu^{2+}OH^{-}\right] \leftrightarrow Cu^{+} + Cu^{2+}O^{-} + H_2O \qquad (2)$$

If Cu(II) remains under the form of the form of a $Cu^{2+}O^{-}$ pair, it becomes undetectable by EPR. The addition of water, in this case, restores the initial oxidation state without any need of molecular oxygen. The above mechanism has been proposed essentially on the basis of the fact that the intensity of Cu(II) EPR spectra drops out upon thermal treatment in vacuum and is restored by simple water adsorption at room temperature. In our case, annealing of EPR samples was not performed under vacuum but in dry synthetic air, keeping this atmosphere for EPR measurements. On the other hand, no control on the

sample atmosphere was made for XPS measurements, what may account for the apparent discrepancy between the two techniques.

On top of this, Palomino et al. [35] propose that the presence of $Cu^{2+}O^{2-}Cu^{2+}$ diamagnetic pairs (S= 0, antiferromagnetic coupling between the two spins) is possible. The existence of such pairs or even of small copper-oxygen clusters has been reported by several authors [37] and would induce EPR silent species.

To sum up, it is not possible to unambiguously clarify with the present data if Cu(II) is really reduced under the annealing in synthetic air as EPR suggest (being this effect not seen by XPS as the atmosphere is not controlled) or if EPR-silent Cu(II) do form on WO_3 and lead to an apparent decrease of Cu(II) species.

As to WO_3:Cu(2%), the magnetic coupling effects were more pronounced and the interaction already occurred on the as-prepared sample; this behaviour is expected from the literature of many different oxide systems [33]. The very slight increase of $g_{\|}$ value and decrease of $A_{\|}$ value observed for the B species suggest an increase in Cu(II) positive charge [39] and/or a decrease in the tetragonal symmetry field distortion around the metal centre due to annealing [40].

3.2.2 Vanadium catalysed WO_3

3.2.2.1 Results

As cited in Chapter 2, vanadium was introduced in different concentrations (0.2, 1, 2 and 5 atomic percentages) and the powders were annealed at two different temperatures (400ºC and 700ºC). Firstly, bulk properties of vanadium catalysed WO_3 powders were analysed by XRD and Raman spectroscopy. As in the previous case, XRD spectra neither displayed significant differences between differently catalysed samples on WO_3 diffraction peaks, nor showed any peak corresponding to a vanadium phase.

Average crystallite size of WO_3 powders was estimated from XRD spectra. Results from the three main crystallographic directions were calculated and they displayed in Fig. 28. It is evident from this figure that, as already noted for copper-catalysed WO_3, the different concentrations of vanadium do not have a significant effect on the crystallite size of the powders. Moreover, the crystallite size remains similar to that of pure WO_3 after the 400ºC-annealing, whereas vanadium-catalysed WO_3 has a slightly higher crystallite size after the 700ºC-annealing.

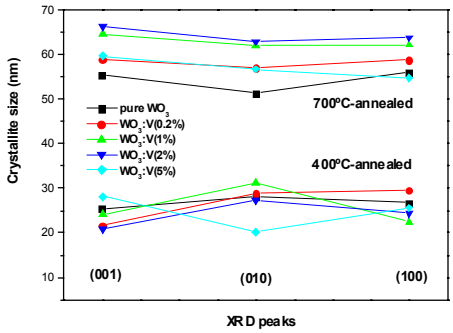

Fig 28: *Crystallite size of WO_3:V powders obtained from the three main crystallographic directions.*

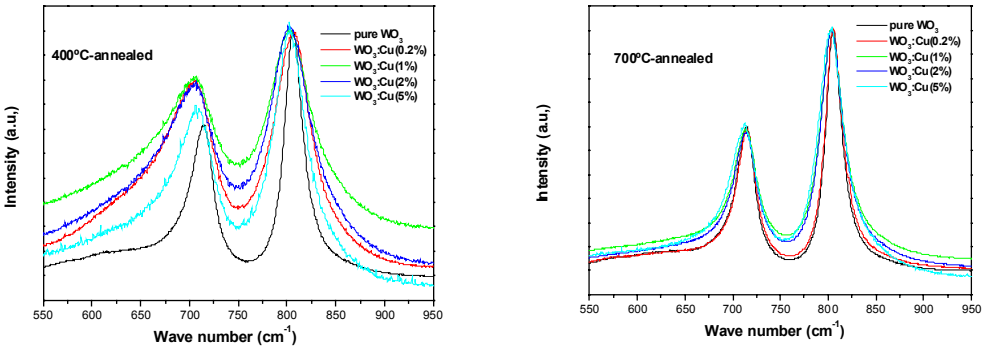

Fig. 29: *Selected region of the Raman spectra of 400ºC-annealed (left-hand) and 700ºC-annealed (right-hand) WO_3:V powders.*

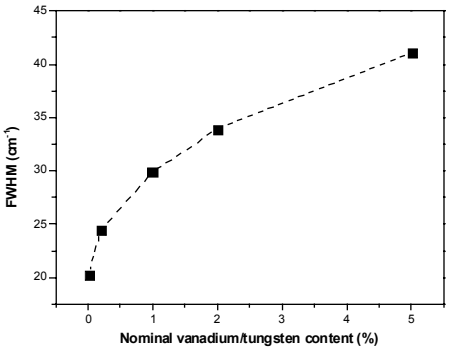

Fig. 30: *Evolution of the FWHM of the 807 cm^{-1}Raman vibration with nominal copper content in 700ºC-annealed WO_3:Cu*

Fig. 29 displays a selected region of the Raman spectra of pure and vanadium-catalysed WO_3. These spectra have been normalised to the maximum intensity of the 807 cm^{-1} vibration mode as already explained. This comparison reveals that, unlike the copper case, both 400ºC and 700ºC-annealed materials have significant variations on the Raman spectra depending on the vanadium content. In the case of 400ºC-annealed powders, the relative intensities of the two peaks vary with chromium content, whereas the 807 cm^{-1} peak of the 700ºC-annealed powders is also depending on vanadium content. This peak has been fitted and the evolution of the FWHM with vanadium content has been analysed (Fig. 30). This figure makes clear that the FWHM increases its value as vanadium content augments.

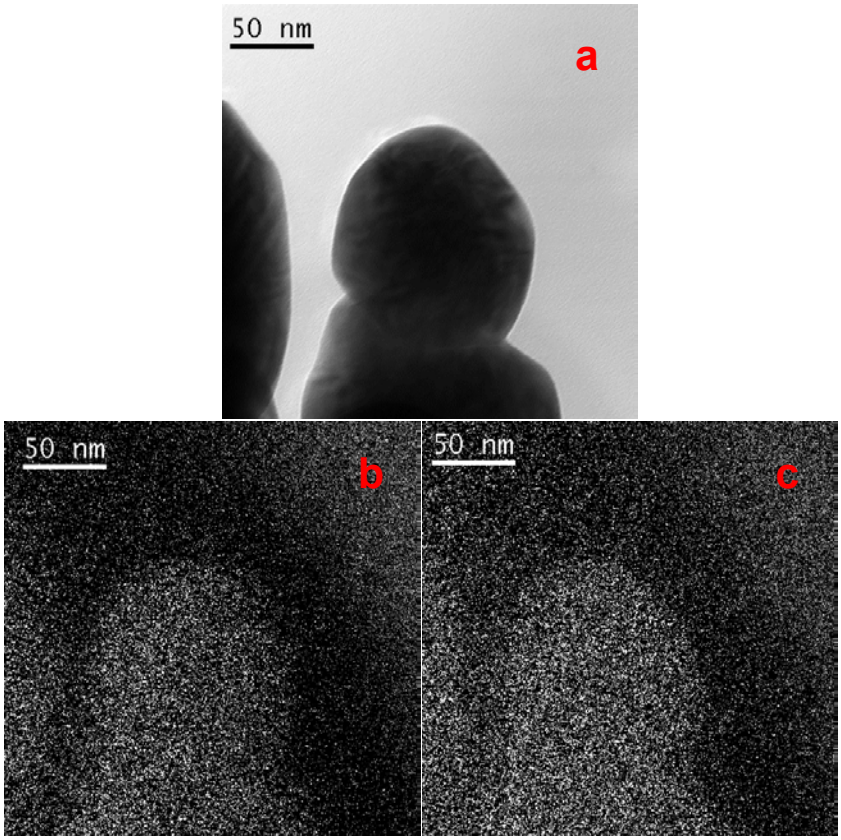

Fig. 31: *(a) TEM image of 700ºC-annealed WO_3:V(5%) grains. (b) Oxygen EELS signal of (a). (c) Vanadium EELS signal of (a).*

The distribution of vanadium on WO_3 powders was firstly investigated by TEM-EELS. Fig. 31a displays a TEM image of 700ºC-annealed WO_3:V(5%), whereas the EELS filtered signal from oxygen and vanadium are displayed in Fig 31b and Fig 31c, respectively. This figure reveals that vanadium is present on WO_3 powders not forming clusters but well-distributed centres.

The chemical state of vanadium was analysed by XPS signal of $V2p_{3/2}$ [41]. No sign of vanadium was found in WO_3:V(0.2%) or 400ºC-annealed WO_3:V(1%). Fig. 32 shows the $V2p_{3/2}$ XPS spectra of 700ºC-annealed vanadium-catalysed WO_3. These spectra were deconvoluted using two peaks and the results are displayed in Table 11. The fitting revealed that there is a major component around 516.9 and 517.5 eV. Although being a rather high variation, it has been reported that the binding energy of V(V) can vary between 516.8 and 517.7 eV[42], so thus is this peak assigned. The second component is found between 516.1 and 516.4 eV and, according to literature, it can be assigned to V(IV) [41-42].

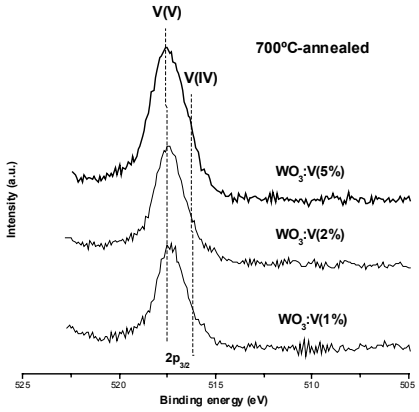

Fig 32: *XPS spectra showing the V $2p_{3/2}$ region for 400ºC annealed WO_3:V.*

		V(IV) BE (eV)	*V(V) BE (eV)*	*V(IV) %*	*V(V) %*	*V/W*
WO_3:V(1%)	**400ºC**	-	-	-	-	-
	700ºC	516.1	517.4	9.9	90.1	0.071
WO_3:V(2%)	**400ºC**	516.1	516.9	9	91	0.005
	700ºC	516.1	517.5	4.2	95.8	0.097
WO_3:V(5%)	**400ºC**	516.2	517.2	3.7	96.3	0.022
	700ºC	516.2	517.5	11.4	88.6	0.133

Table 11: *Results of peak deconvolution of the vanadium photoelectron signal after calcination*

This data make clear that vanadium is mainly in its highest oxidation state for all the samples analysed. As annealing temperature increases from 400ºC to 700ºC, some V(IV) seems to oxidise to V(V) for WO_3:V(2%), whereas the reverse process is apparently occurring for WO_3:V(5%). As to the surface concentration of vanadium, it is interesting to

notice that the V/W ratio is clearly higher for 700ºC-annealed samples. Finally, EPR was utilised to investigate the WO_3:V(0.2%) sample, taking advantage of its higher sensitivity compared to XPS. Unfortunately, the application of this technique to the study of vanadia species is limited in practice to the detection of the spectra due to V(IV) ions [43], since only these vanadium species is paramagnetic. Furthermore, the spectra of V(IV) are actually complicated by the high number of hyperfine levels (the levels generated by the interaction of the unpaired electron with the I=7/2 ^{51}V nucleus) and by the second order effects that tend to produce an asymmetric hyperfine structure with unequal separation of the various lines. However, it can provide a detailed description of the specific nature of the V(IV) species (V^{4+} or VO^{2+}) and of their co-ordination which proves extremely useful for a deep understanding of the whole system.

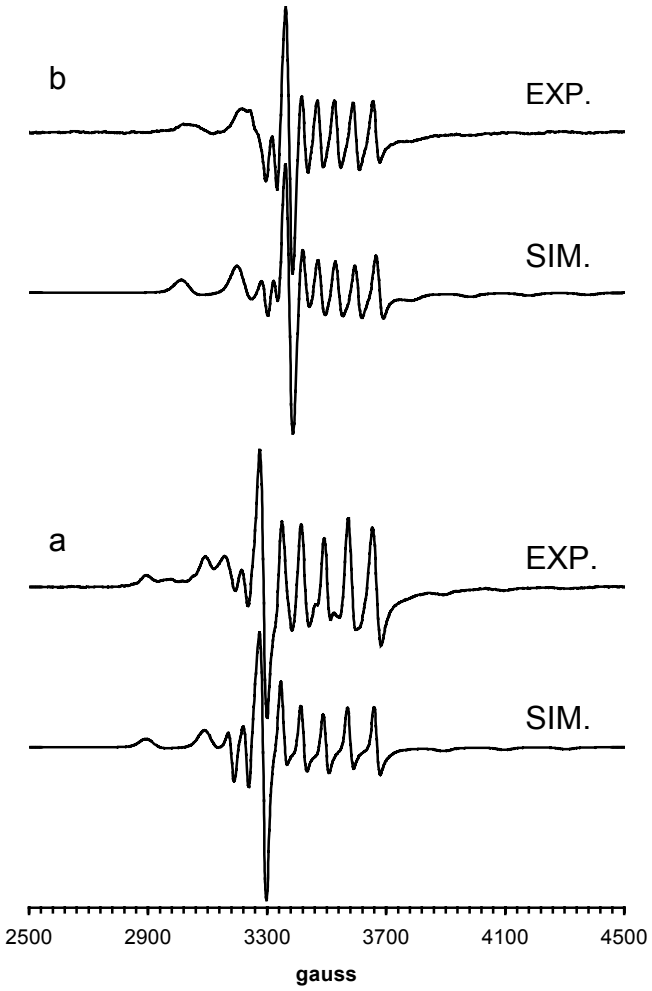

Fig. 33: *Experimental and simulated and EPR spectra, recorded at 123 K, of WO_3:V(0.2%) samples (a) as-prepared (b) annealed at 400°C.*

The EPR spectrum of the as-prepared WO_3:V(0.2 %) sample showed well resolved resonance lines (Fig. 33) attributable to magnetically isolated V(IV) centres (species A) in an axial symmetry field of oxygen centres, with $g_{\parallel} = 1.870$, $g_{\perp} = 1.961$, $A_{\parallel} = 202$ G $A_{\perp} = 69$ G. Samples annealed at 400°C showed a different V(IV) centre (species B) with $g_{\parallel} = 1.821$, $g_{\perp} = 1.926$, $A_{\parallel} = 195$ G $A_{\perp} = 53.8$ G. Species B was also observed after the annealing at 700°C, though in a much lower amount.

The spin hamiltonian parameters of A and B species gave a detailed structural description of tetravalent vanadium centres. According to Davidson and Che [43], the average values of g and A principal components of the species A, g_{iso}= 1.931 and A_{iso}=113 G, indicated that V(IV) ions were in form of VO^{2+}. On the other hand, g_{iso}= 1.891 and A_{iso}=101 G of the species B were typical of tetracoordinated V^{4+} ions, probably located in the interstitial sites of WO_3 lattice [44].

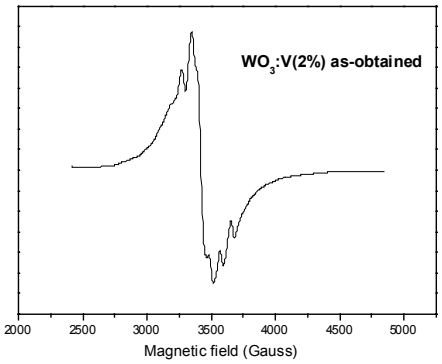

Fig. 34: *Experimental EPR spectrum, recorded at 123 K, of as-obtained WO_3:V(2%).*

Fig. 34 displays the EPR spectra of as-obtained WO_3:V(2%). It is evident from this figure that a new species (C) appears. This species is due to interacting V(IV) centres and becomes significant as the amount of vanadium increases. The magnetic interaction is large enough to mask the hyperfine structure and to produce a broad line.

Species	$g_{\parallel}$	$g_{\perp}$	g_{av}	$A_{\parallel}$	$A_{\perp}$	
A	1.870	1.961	1.931	202.0	69.0	113.3
B	1.821	1.926	1.891	195.0	53.8	100.9
C	-	-	1.980	-	-	unres

Table 12: *EPR parameters of WO_3:V obtained from simulations.*

Finally, the V(IV) amount decreased by increasing the temperature of the oxidative treatment for both WO_3:V(2 %) and WO_3:V(0.2 %) samples. In particular, only traces of V(IV) were observed after the 700ºC-annealing in synthetic air.

3.2.2.2 Discussion

As revealed by Raman spectroscopy, there is a distortion on the O-W-O vibration (according to the increasing FWHM) that is correlated with the vanadium nominal content. Since this is detected in 700ºC-annealed powder, it means that this may not be just a superficial effect as in the case of Cu on WO_3. This effect may be related to the EPR data, which attribute a paramagnetic vanadium species to V^{4+} ions in tetrahedral bulk sites of the WO_3 matrix, as pointed out in [44]. Actually, this species was only detected after the annealing (either at 400ºC or 700ºC), what would favour their insertion into the bulk.

From XPS data, it is clear that V(V) is the major species on the surface of WO_3. According to Weckhuysen et al. [45], this is the typical scenario that can be found when NH_4VO_3 is dissolved in an aqueous oxalic acid solution as a precursor of vanadium species. The impregnation process is followed by a drying and heating step in which the vanadium oxide compound is chemically anchored onto the support metal oxide (Fig. 35).

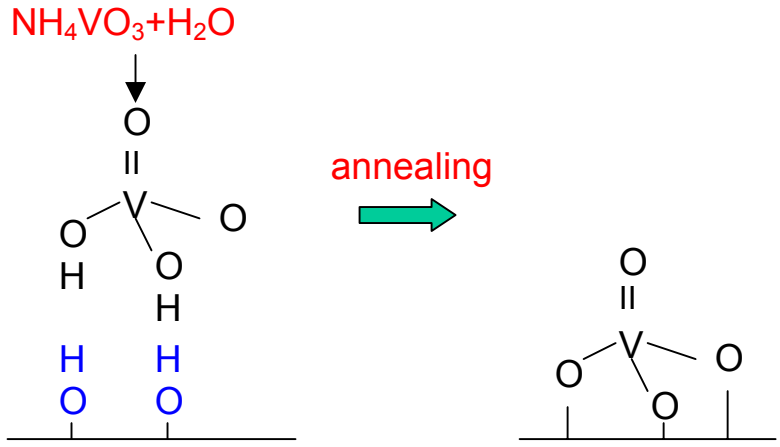

Fig. 35: *Synthesis method of WO_3:V by impregnation with an aqueous solution of NH_4VO_3 followed by annealing in air. (Adapted from 45).*

This figure displays that, upon heating, the water molecules adsorbed on the support (WO_3) and around the supported vanadium oxides are removed and vanadium centres are oxidised

to V(V). At low surface vanadium loading, the most common vanadium species is supposed to be this isolated VO_4 units, containing one terminal mono-oxo V=O bond and three bridging vanadium-oxygen-tungsten oxide bond with symmetry C_{3v} [45]. However, with increasing surface vanadium loading, polymeric chains of VO_4 units may appear. This is probably the case of 700ºC-annealed powders, where the surface V/W ratio is clearly higher than in 400ºC-annealed samples. This effect is clearly due to a reduction on the number of apparent superficial W atoms as annealing temperature increases due to grain growth. This is further supported by the binding energy of the V(V) $2p_{3/2}$, since it has a lower value for 400ºC-annealed samples. According to Reiche et al. [46], annealing at high temperatures is reported to increase the positive charge of the catalytic metal, due to the loss of residual OH groups around it and thus Binding Energy (BE) value increases too.

Finally, EPR indicated the presence of superficial vanadylic ions $(VO)^{2+}$. This means that one of the vanadium-oxygen bonds is particularly short and can be described in terms of a double V=O bond. Since this species have been detected in dry air, it is possible that they lead to the formation of V-OH after contact with ambient air [44]. This is a key point to understand the Brønsted acidity exhibited by vanadium-supported materials, as discussed in Chapter 5.

3.2.3 Chromium catalysed WO_3

3.2.3.1 Results

As already explained in Chapter 2, chromium was introduced in different concentrations (0.2, 1, 2 and 5 atomic percentages) and the powders were annealed at two different temperatures (400ºC and 700ºC). As proceeded above, bulk properties of vanadium catalysed WO_3 powders were analysed by XRD and Raman spectroscopy. XRD spectra displayed neither significant difference between differently catalysed samples on WO_3 diffraction peaks, nor showed any peak corresponding to a chromium phase.

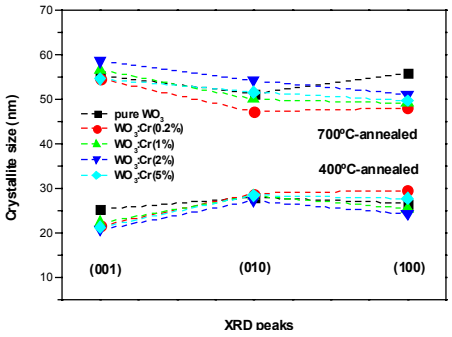

Fig 36: *Crystallite size of WO_3:Cr powders obtained from the three main crystallographic directions.*

Crystallite size was calculated from the three main crystallographic directions (Fig. 36). It is evident from this figure that, as already noted before for copper and vanadium, the different concentrations of chromium do not have a significant effect on the crystallite size of the powders. Moreover, the crystallite size remains similar to that of pure WO_3 after the 400ºC and 700ºC-annealing.

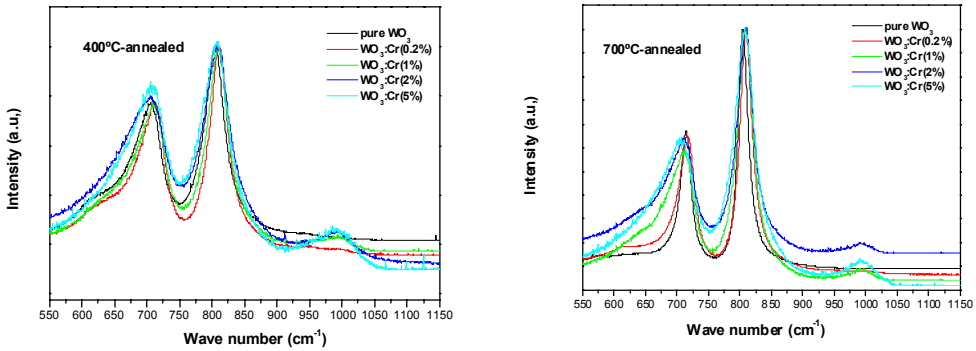

Fig. 37: *Selected region of the Raman spectra of 400ºC-annealed (left-hand) and 700ºC-annealed (right-hand) WO_3:Cr powders.*

Fig. 37 displays a selected region of the Raman spectra of pure and chromium-catalysed WO_3. These spectra have been normalised to the maximum intensity of the 807 cm^{-1} vibration mode as already mentioned. This comparison reveals that, similarly to the

vanadium case, both 400ºC and 700ºC-annealed materials have significant variations on the Raman spectra depending on the chromium content, especially in the shape of the peaks. This point is clearly displayed in Fig. 38, where the normalised FWHM of the 807 cm^{-1} of the 400ºC and 700ºC-annealed powders. This peak has been fitted and the evolution of the FWHM with chromium content has been analysed and normalised to the value of pure WO_3 for each annealing temperature. As in the case of vanadium, this figure makes clear that the FWHM increases its value as chromium content augments.

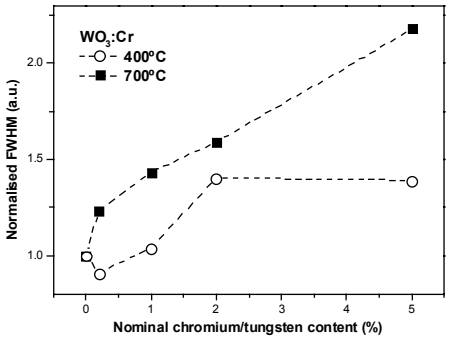

Fig. 38: *Evolution of the FWHM of the 807 cm^{-1}Raman vibration with nominal copper content in 400ºC and 700ºC-annealed WO_3:Cr*

Interestingly, the previous figure displayed a new Raman vibration centred on 990 cm^{-1}. Fig. 39 presents a detailed view of the Raman scattering in the 850-1100 cm^{-1} region for 0.2% and 2% chromium-catalysed WO_3 (as-prepared, 400ºC-annealed and 700ºC-annealed). It is well known that this region is of particular interest since terminal M=O vibrations of transition metal are present in the 900-1000 cm^{1} zone [47]. Fig. 39 indicates that two Raman vibration modes are present. The one centred at 947 cm^{-1} is noticeable in as-prepared and, as a shoulder, in 400ºC-annealed materials. This vibration is due to W=O groups and, as put forward in previous studies [9] and in section 3.1.1.2, disappears as annealing temperature raises due to a recrystallisation and/or grain growth.

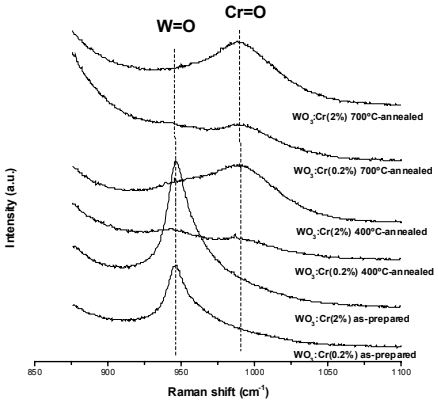

Fig. 39: *Selected region of the Raman spectra of 0.2 and 2% chromium -catalysed WO_3*

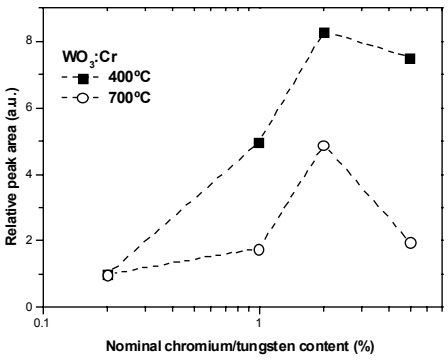

Fig. 40: *Relative 990 cm^{-1}-peak area evolution with nominal chromium concentration.*

More interesting is the vibration centred around 990 cm^{-1} since, according to Weckhuysen et al. [48], it may come from dehydrated monochromate Cr=O vibrations. After correcting the baseline (due to the intense O-W-O vibration at 807 cm^{-1}) and deconvoluting the peak, the evolution of the area of this vibration with nominal chromium content is shown in Fig. 40. The area has been normalised to the area of WO_3:Cr(0.2%) for each annealing temperature. This figure makes clear that the area of this vibration is correlated with nominal chromium content but for the case of WO_3:Cr(5%), where there is a reduction in the area of the 990 cm^{-1} vibration.

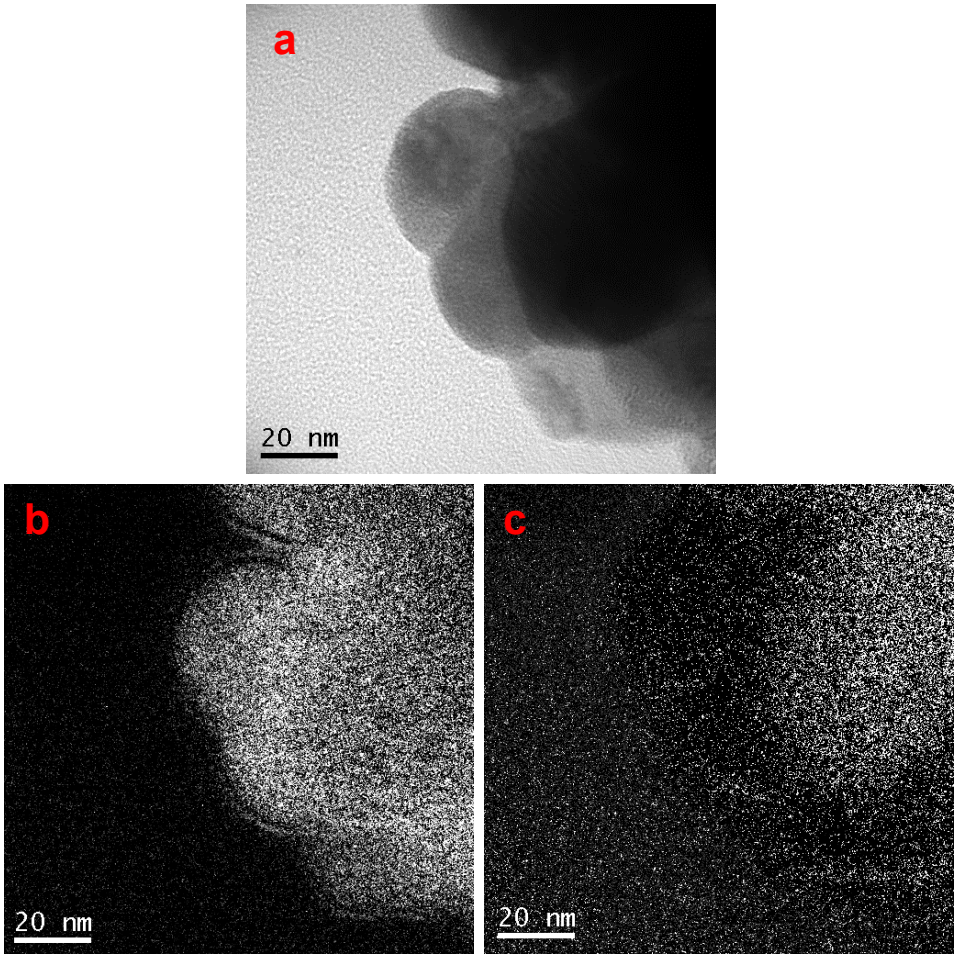

Fig. 41: *(a) TEM image of 700ºC-annealed WO_3:Cr(5%) grains. (b) Oxygen EELS signal of (a). (c) Chromium EELS signal of (a).*

Fig. 41a, 41b and 41c show a TEM image of 700ºC-annealed WO_3:Cr(5%) particles, an EELS image of oxygen atoms and an EELS image of chromium atoms present in these particles, respectively. Chromium centres seem to be more present to the right-hand of the image, which is probably due to a higher concentration of grains on that side of the image. These figures illustrate that chromium is dispersed on WO_3 grains and that no chromium clusters are present on this material.

The chemical state of chromium centres was analysed by the XPS signal of the Cr $2p_{3/2}$ region [48]. Due to XPS detection limits, no chromium signal was detected in the case of WO_3:Cr(0.2%) samples.. Fig. 42 displays the Cr $2p_{3/2}$ XPS spectra of 400ºC-annealed chromium-catalysed WO_3. These spectra were deconvoluted using two peaks and the results are displayed in Table 13. As-prepared and 400ºC-annealed powders presented two contributions, whereas 700ºC-annealed samples only presented one. Table 13 also shows the total chromium peak area normalised to the tungsten peak area and the relative concentration of the peak found in as-prepared and 400ºC-annealed materials (obtained from the area of the its fitting peak and normalised to the total chromium peak area).

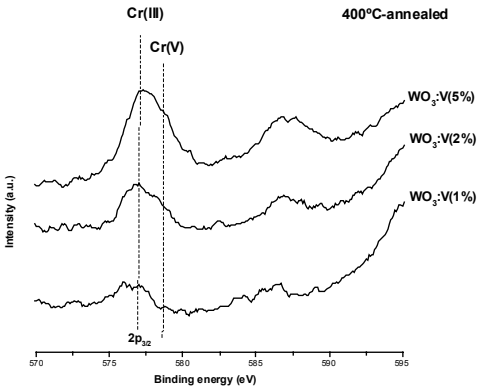

Fig 42: *XPS spectra showing the Cr $2p_{3/2}$ region for 400ºC annealed WO_3:Cr.*

The common peak to all chromium-catalysed WO_3 powders was found to have a BE between 576.9 and 577.2 eV. According to reported values of supported chromium species [48-50], these BE's are typical of Cr(III). The second peak appearing in as-prepared and 400ºC-catalysed samples is centred between 578.5 and 578.9 eV and its nature is not so straightforward to ascribe. Although Cr(VI) is a very common species when dealing with chromium supported on metal oxides, its BE value is frequently around 580 eV, what indicates our species is not likely to be Cr(VI). On the other hand, Cr(V) is reported to have its BE around 579 eV [48], and so this species is assigned. Its relative concentration is given in Table 13. These data indicate that the relative concentration of Cr(V) decreases after the annealing at 400ºC, which would agree with its disappearance after the 700ºC-

annealing. On the other hand, little correlation is found between nominal chromium concentration and presence of Cr(V). Finally, Cr surface content (normalised to W surface content) has an apparent decrease as annealing temperature decreases.

		Cr(III) BE (eV)	*Cr(V) BE (eV)*	*Cr(III) %*	*Cr(V)%*	*Cr/W*
WO_3:Cr(1%)	**a.p.**	577.1	578.51	57	43	0.029
	400ºC	577.1	578.5	86	14	0.009
	700ºC	577.1	-	100	-	0.012
WO_3:Cr(2%)	**a.p.**	576.9	578.56	70	30	0.039
	400ºC	576.9	578.6	71	29	0.017
	700ºC	577.0	-	100	-	0.013
WO_3:Cr(5%)	**a.p.**	577.2	578.79	70	30	0.070
	400ºC	577.0	578.7	67	33	0.050
	700ºC	577.1	-	100	-	0.020

Table 13: *Results of XPS peak deconvolution of the chromium photoelectron signal after calcination*

EPR characterisation of these samples showed the presence of interacting Cr(III) centres. The magnetic interaction was large enough to mask the hyperfine structure and thus to avoid a fine study.

3.2.3.2 Discussion

As indicated by Raman spectroscopy, and in much the same way as in WO_3:V, there is a distortion on the O-W-O vibration (according to the increasing FWHM) that is correlated with the chromium nominal content. Interestingly, the distortion seems to be higher for 700ºC-annealed powders, what may indicate that more chromium has diffuse to the bulk of WO_3 as annealing temperature was risen from 400ºC to 700ºC. This also may account for the lowest superficial concentration of Cr detected by XPS as annealing temperature increases. However, the lost of chromium in the drying-annealing process can not be ruled out.

As to the arrangement of chromium species on the surface of WO_3, XPS data revealed that most superficial chromium species are Cr(III) centres. Besides, Raman spectroscopy has confirmed the presence of monochromate Cr=O groups. Due to the nature of this

chromium-oxygen bond, it seems clear that these must be terminal groups, i.e. superficial. Furthermore, EELS images indicate that chromium is not forming clusters (there is not Cr_2O_3) but rather dispersed centres. Taking these points into account, chromium could be distributed on the surface as displayed in Fig. 43 (left-hand). This configuration was proposed by Terano et al. [50]. However, comparison of the Raman Cr=O peak area (Fig. 40) indicated a falling-off in the presence of this group as chromium concentration increased. This may be a clear example of the formation of polychromate species that occur as chromium content increases [48]. Since chromium remains essentially as Cr(III), a second possible configuration is also displayed in Fig. 43 (right-hand) [50].

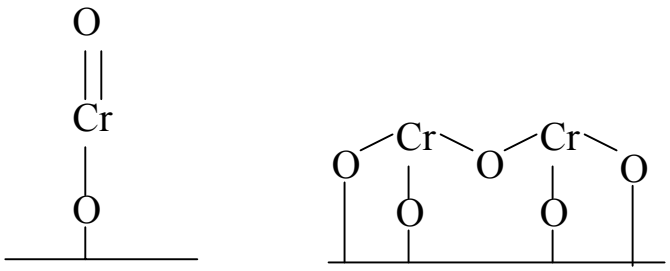

Fig. 43: *Plausible structures of surface-stabilised chromium species ($Cr(III)O_x$). (Adapted from [50]).*

3.2.4 Conclusions

Finally, the main conclusions that can be drawn from the above-presented experimental data on catalysed WO_3 nanocrystalline powders are:

- Crystallite size and grain size and shape is not considerably affected by the addition of copper, vanadium and chromium using this experimental procedure.
- According with XRD data, additives form neither a separate crystalline phase, nor cause noticeable distortions to the WO_3 bulk crystalline phase. On the other hand, main Raman WO_3 vibration was affected by additive addition as revealed by the variation of the FWHM. This parameter increased as vanadium and chromium content grew. This may indicate that additives do diffuse to the bulk and, at least, the outermost layers of tungsten oxide are slightly distorted. Surprisingly, increasing copper content made FWHM decrease its value, being its reason unclear.

- Copper was present on the surface of particles as Cu(II) and, mainly, as reduced copper, probably Cu(I), according to XPS data. The surface Cu/W ratio was between 0.008 and 0.017.
- EPR revealed that Cu(II) were well distributed on WO_3 as their concentration was low and that copper ions approached as annealing temperature increased. EPR data also suggest that, under controlled annealing in pure air, Cu(II) is reduced to Cu(I), probably due to the dehydroxylation of the sample. However, the appearence of Cu(II) EPR-silent species should not be ruled out.
- TEM-EELS characterisation indicated that vanadium was well distributed (without forming clusters) on WO_3.
- Vanadium centres were mainly V(V), with V(IV) also present in a small fraction, according to XPS data. The superficial concentration of vanadium (V/W) was in the range 0.071-0.133, with a clear rise as annealing temperature increased.
- V(IV) centres were detected by EPR, showing that they can be present as V^{4+} (bulk) and VO^{2+} (surface) centres. As annealing temperature increased in pure synthetic air, their concentration fell off.
- Raman investigations revealed that Cr=O vibrations were present in chromium catalysed samples, probably due to monochromate superficial species.
- Chromium centres were well distributed on WO_3, according to TEM-EELS investigation.
- Surface chromium centres were mainly Cr(III), although Cr(V) was present in as prepared and 400ºC-annelaed samples. The Cr/W superficial ratio varied between 0.029 and 0.070, with a clear reduction as annealing temperature increased.

3.4 References

[1] M.F. Daniel, B. Desbat, J.C. Lassegues, B. Gerand and M. Figlarz, *Infrared and Raman study of WO_3 tungsten trioxides and WO_3:xH_2O tungsten trioxides hydrates*, J. Solid State Chem. 67 (1987) 235-247.

[2] J. H. Kim and K. L. Kim, *A study of preparation of tungsten nitride catalysts with high surface area*, Appl. Catal. A 181 (1999) 103-111.

[3] P.Woodward, A. Sleight, T. Vogt, *Structure refinement of triclinic tungsten trioxide*, J. Phys. Chem. Solids 56 (1995) 1035-1315.

[4] Rodriguez-Carvajal, J.Powder diffraction, Abstracts of the Satellite meeting of the XV congress of the International Union of Crystallography, Toulouse 16-19 July, 1990, 127 L.

[5] E. Cazzanelli, C. Vinegoni, G. Mariotto, A. Kuzmin, J. Purans, *Low-temperature polymorphism in tungsten trioxide powders and its dependence on mechanical treatments*, J. Sol. State Chem. 143 (1999) 24-32.

[6] P. Scherrer, Gôttinger Nachr. 2 (1918) 98.

[7] M.F. Daniel, B. Desbat, J.C. Lassegues, B. Gerand and M. Figlarz, *Infrared and Raman study of WO_3 tungsten trioxides and WO_3,xH_2O tungsten trioxides hydrates*, J. Solid State Chem. 67 (1987) 235-247.

[8] A. Takase and K. Miyakawa, *Raman Study on sol-gel derived tungsten oxide from tungsten ethoxide*, Jpn. J. Appl. Phys., 30 (1991) L 1508-1511.

[9] C. Bittencourt, R. Landers, E. Llobet, G. Motas, X. Correig, M. Silva, J. Sueiras, J. Calderer, *Effects of oxygen partial pressure and annealing temperature on the formation of sputtered tungsten oxide films*, J. Electrochem. Soc. 149 (2002) H81-H86.

[10] E. Salje, Acta crystallogr. Sect. A 31 (1975) 360.

[11] E. Cazzanelli, C. Vinegoni, G. Mariotto, A. Kuzmin, J. Purans, *Low-temperature polymorphism in tungsten trioxide powders and its dependence on mechanical treatments*, J. Sol. State Chem. 143 (1999) 24-32.

[12] A. Souza-Filho, V. Freire, J. Sasaki, J. Mendes-Filho, J. Juliao, U. Gomes, *Coexistence of triclinic and monoclinic phases in WO_3 ceramics*, J. Raman Spect. 31 (2000) 451-454.

[13] J. Solis, S. Saukko, L. Kish, C. Granqvist, V. Lantto, *Nanocrystalline tungsten oxide thick-films with high sensitivity to H_2S at room temperature*, Sens. Actuators B 77 (2001) 316-321.

[14] R. D. Bringans, H. Höchst, H. R. Shanks, *Defect states in WO_3 studied with photoelectron spectroscopy*, Phys. Rev. B 24 (1981) 3481

[15] S. Santucci, C. Cantalini, M. Crivellari, L. Lozzi, L. Ottaviano, M. Passacantando, *X-ray photoemission spectroscopy and scanning tunnelling spectroscopy study on the thermal stability of WO_3 thin films*, J. Vac. Sci. Technol. A 18 (2000) 1077-1082.

[16] S. Santucci, L. Lozzi, E. Maccallini, M. Passacantando, L. Ottaviano, *Oxygen loss and recovering induced by ultrahigh vacuum and oxygen annealing on WO_3thin film surfaces: influences on the gas response properties*, J. Vac. Sci. Technol. A 18 (2000) 1077-1082.

[17] H. Sun, C. Cantalini, L. Lozzi, M. Passacantando, S. Santucci, M. Pelino, *Microstructural effect on NO_2 sensitivity of WO_3 thin film gas sensors*, Thin Solid Films 287 (1996) 258-265.

[18] K. Kosuge, *Chemistry of non-stoichiometric compounds*, p. 120, Oxford University Press, Oxford, 1994.

[19] J. Sloan, J. Hutchison, R. Tenne, Y. Feldman, T. Tsirlina, M. Homyonfer, *Defect and ordered tungsten oxides encapsuled inside 2H-WX_2 fullerene-related structures*, J. Solid State Chem. 144 (1999) 100-117.

[20] J.G. Allpress, R.J.D. Tilley, M.J. Sienko, *Examination of substoichiometric WO_{3-x} crystals by electron microscopy*, J. Sol. State Chem. 3 (1971) 440-451.

[21] G. Ramis, C. Crstiani, A. Elmi, P. Villa, *Characterization of the surface properties of polycrystalline WO_3*, J. Mol. Catal. 61 (1990) 319-331

[22] C. Bittencourt, R. Landers, E. Llobet, X. Correig, J. Calderer, *The role of oxygen partial pressure and annealing temperature on the formation of W=O bonds in thin WO_3 film*, Semicond. Sci. and Technol. 17 (2000) 522-525.

[23] Cs. Balázsi, M. Farkas-Jahnke, I. Kotsis, L. petrás, J. Pfeifer, *The observation of cubic tungsten trioxide at high-temperature dehydration of tungstic acid hydrate*, Solid State Ionics 141-142 (2001) 411-416

[24] S. Kanan, Z. Lu, J. Cox, G. Bernhardt, C. Tripp, *Identification of surface sites on monoclinic WO_3 powders by infrared spectroscopy*, Langmuir 18 (2002) 1707-1712.

[25] A. Tocchetto, A, Glisenti, *Study of the interaction between simple molecules and W-Sn based oxide catalysts. 1. The case of WO_3 powders*, Langmuir 16 (2000) 6173-6182.

[26] C. Baertsch, S. Soled, E. Iglesia, *Isotopic and chemical titration of acid sites in tungsten oxide domains supported on zirconia*, J. Phys. Chem. B 105 (2001) 1320-1330.

[27] C. Guéry, C. Choquet, F. Dujeancourt, J. Tarascon, J. Lassègues, *Infrared and X-ray studies of hydrogen intercalation in different tungsten trioxides and tungsten trioxide hydrates*, J. Solid State Electrochem. 1 (1997) 199-207.

[28] G. Bamwenda, H. Arakawa, *The visible light induced photocatalytic activity of tungsten trioxide powders*, Appl. Catal. A 210 (2001) 181-191.

[29] M.M.J. Treacy, J.M. Newsam, M.W. Deem Porc., R. Soc. Lond. A (1991) 433, 499-520.

[30] B. Wen, M. He, *Study of the Cu-Ce synergism for NO reduction with CO in the presence of O_2, H_2O and SO_2 in FCC operation*, Appl. Catal. B 37 (2002) 75-82.

[31] W. Liu, M. Flytzani-Stephanopoulos, *Total oxidation of carbon monoxide and methane over transition metal-fluorite oxide composite catalysts*, J. Catal. 153 (1995) 317-332.

[32] C. Fernando, P. Silva, S. Wethasinha, I. Dharmadasa, T. Delsol, M. Simmonds, *Investigation of n-type Cu_2O layers prepared by a low cost chemical method for use in photo-voltaic thin film solar cells,* Renew, Energy 26 (2002) 521-529.

[33] J.Peisach, W.E.Blumberg, Arch. Biochem. Biophys., 165, 691 (1974).

[34] V.Indovina, M.Occhiuzzi, D.Pietrogiacomi, S.Tuti, J.Phys.Chem. B, 103, 9967 (1999).

[35] Gemma Turnes Palomino, Paola Fisicaro, Silvia Bordiga, and Adriano Zecchina Elio Giamello and Carlo Lamberti, *Oxidation States of Copper Ions in ZSM-5 Zeolites. A Multitechnique Investigation,* J. Phys. Chem. B 104 (2000) 4064-4073.

[36]Hollemann-Wiberg, Inorganic Chemistry, Nils Wiberg Ed.(2001) Academic Press, pg. 1388 and following, pg. 1253.

[37] H.-J. Jang, W. Keith Hall, Julie L. d'Itri, *Redox Behavior of CuZSM-5 Catalysts: FTIR Investigations of Reactions of Adsorbed NO and CO,* J. Phys. Chem 100 (1996) 9416.

[38] T. Beutel, J. Sárkány, G.-D. Lei, J. Y. Yan, and W. M. H. Sachtler, *Redox Chemistry of Cu/ZSM-5,* J. Phys. Chem. 100 (1996) 397.

[39] M. A. Reiche, T. Bürgi, A. Baiker, A. Scholz, B. Schnyder and A. Wokaun, Appl. Catal. A 198 (2000) 155-169.

[40] V.Bassetti, L.Burlamacchi, G.Martini, J.Am.Chem.Soc., 101, 5471 (1979).

[41] M. Shin, C. Nam, D. Park, J. Chung, *Selective oxidation of H_2S to elemental sulfur over VO_x/SiO_2 and V_2O_5 catalysts*, Appl. Catal. 211 (2001) 213-225.

[42] J. Keränen, A. auroux, S. Ek, L. Niinistö, *Preparation, characterization and activity testing of vanadia catalysts deposited onto silica and alumina supports by atomic layer deposition*, Appl. Catal. 228 (2002) 213-225.

[43] A.Davidson, M.Che, *Temperature-induced diffusion of probe vanadium (IV) ions into the matrix of titanium dioxide as investigated by ESR technique*, J.Phys.Chem. 96, 9909 (1992).

[44] M.C.Paganini, L.Dall'Acqua, E.Giamello, L.Lietti, P.Forzatti, G.Busca, *An EPR study of the surface chemistry of the V_2O_5-WO_3/TiO_2 catalyst: redox behaviour and state of V(IV)*, J. Catal., 166, 195 (1997).

[45] Bert M. Weckhuysen., Daphne E. Keller, *Chemistry, spectroscopy and the role of supported vanadium oxides in heterogeneous catalysis*, Catalysis Today 78 (2003) 25–46.

[46] M. A. Reiche, T. Bürgi, A. Baiker, A. Scholz, B. Schnyder and A. Wokaun, *Vanadia and tungsta grafted on TiO_2: influence of the grafting sequence on structural and chemical properties*, Appl. Catal. A 198 (2000) 155-169.

[47] I. Wachs, *Raman and IR studies of surface metal oxide species on oxide supports: Supported metal oxide catalysts*, Catalysis Today 27 (1996) 437-455.

[48] B. Weckhuysen, I. Wachs, R. Schoonheydt, *Surface Chemistry and Spectroscopy of Chromium in Inorganic Oxides*, Chem. Rev. 96 (1996) 3327-3349.

[49] P. Harrison, N. Lloyd, W. Daniell, I. Ball, C. Bailey, W. Azelee, *Evolution of Microstructure during the thermal activation of copper(II) and chormium(III) doubly promoted tin(IV) oxide catalysts: an FT-IR, XRD, TEM, XANES/EXAFS, and XPS study*, Chem. Mater. 12 (2000) 3113-3122.

[50] B. Liu, M. Terano, *Investigation of the physico-chemical state and aggregation mechanism of surface Cr species on a Philips CrO_x/SiO_2 catalyst by XPS and EPMA*, J. Molec. Catal. A 172 (2001) 227-240.